**RESEARCH ARTICLE**

# Characteristics and effects of aerosols during blowing snow events in the central Arctic

Nora Bergner[1] ⓘ, Benjamin Heutte[1], Ivo Beck[1], Jakob B. Pernov[1,2], Hélène Angot[1,3], Stephen R. Arnold[4], Matthew Boyer[5], Jessie M. Creamean[6], Ronny Engelmann[7], Markus M. Frey[8], Xianda Gong[9,10], Silvia Henning[7], Tamora James[4], Tuija Jokinen[5,11], Gina Jozef[12,13,14], Markku Kulmala[5], Tiia Laurila[5], Michael Lonardi[1], Amy R. Macfarlane[15,16], Sergey Y. Matrosov[13,17], Jessica A. Mirrielees[18], Tuukka Petäjä[5], Kerri A. Pratt[18,19], Lauriane L. J. Quéléver[5], Martin Schneebeli[20], Janek Uin[21], Jian Wang[22], and Julia Schmale[1],*

Sea salt aerosol (SSaer) significantly impacts aerosol-radiation and aerosol-cloud interactions, and sublimated blowing snow is hypothesized to be an important SSaer source in polar regions. Understanding blowing snow and other wind-sourced aerosols' climate relevant properties is needed, especially during winter when Arctic amplification is greatest. However, most of our understanding of blowing snow SSaer comes from modeling studies, and direct observations are sparse. Additionally, SSaer can originate from multiple sources, making it difficult to disentangle emission processes. Here, we present comprehensive observations of wind-sourced aerosol during blowing snow events from the Multidisciplinary drifting Observatory for the Study of Arctic Climate (MOSAiC) expedition in the central Arctic. High wind speed strongly enhances total aerosol number, submicron sodium chloride mass, cloud condensation nuclei concentrations, and scattering coefficients. Generally, the relative response of aerosol properties to wind speed enhancement is strongest in fall when Arctic aerosol concentrations are lowest. Blowing snow events showed similar aerosol and environmental properties across events, apart from occasions with high snow age (>6 days since last snowfall). Coarse-mode number concentrations (>1 μm) are better explained by variability in wind speed averaged over 12-h air mass back trajectories arriving at the MOSAiC site compared to local, instantaneous wind speed, suggesting the importance of regional transport and consideration of air mass

[1] Extreme Environments Research Laboratory, Ecole Polytechnique Fédérale de Lausanne (EPFL) Valais Wallis, Sion, Switzerland

[2] Current address: School of Earth and Atmospheric Sciences, Queensland University of Technology, Brisbane, Australia

[3] Univ. Grenoble Alpes, CNRS, INRAE, IRD, Grenoble INP, IGE, Grenoble, France

[4] School of Earth and Environment, University of Leeds, Leeds, UK

[5] Institute for Atmospheric and Earth System Research/INAR-Physics, Faculty of Science, University of Helsinki, Helsinki, Finland

[6] Department of Atmospheric Science, Colorado State University, Fort Collins, CO, USA

[7] Leibniz Institute for Tropospheric Research, Leipzig, Germany

[8] Natural Environment Research Council, British Antarctic Survey, Cambridge, UK

[9] Research Center for Industries of the Future, Westlake University, Hangzhou, China

[10] Key Laboratory of Coastal Environment and Resources of Zhejiang Province, School of Engineering, Westlake University, Hangzhou, China

[11] Climate & Atmosphere Research Centre (CARE-C), The Cyprus Institute, Nicosia, Cyprus

[12] Department of Atmospheric and Oceanic Sciences, University of Colorado Boulder, Boulder, CO, USA

[13] Cooperative Institute for Research in Environmental Sciences, University of Colorado, Boulder, CO, USA

[14] National Snow and Ice Data Center, University of Colorado Boulder, Boulder, CO, USA

[15] Earth Observation Group, UiT The Arctic University of Norway, Tromsø, Norway

[16] Geography and Environmental Sciences, Northumbria University, Newcastle, UK

[17] National Atmospheric and Oceanic Administration, Physical Sciences Laboratory, Boulder, CO, USA

[18] Department of Chemistry, University of Michigan, Ann Arbor, MI, USA

[19] Department of Earth and Environmental Sciences, University of Michigan, Ann Arbor, MI, USA

[20] WSL Institute for Snow and Avalanche Research, Davos Dorf, Switzerland

[21] Environmental and Climate Sciences Department, Brookhaven National Laboratory, Upton, NY, USA

[22] Center for Aerosol Science and Engineering, Department of Energy, Environmental and Chemical Engineering, Washington University in St. Louis, St. Louis, MO, USA

* Corresponding author:
Email: julia.schmale@epfl.ch

history for wind-driven aerosol production. These MOSAiC observations provide new insights into wind-driven aerosol in the central Arctic and may help validate modeling studies and improve model parameterizations particularly for aerosol direct and indirect radiative forcing.

---

**Keywords:** Arctic, Atmosphere, Wind-sourced aerosol, Blowing snow, MOSAiC

---

## 1. Introduction

The Arctic is rapidly changing in response to climate change, experiencing surface temperature increases, which are 3 to 4 times higher compared to the global mean and lower latitudes (Rantanen et al., 2022, time period 1979–2021). The accelerated warming, also referred to as Arctic amplification, has profound implications for natural systems and humans locally and globally (Hovelsrud et al., 2011; Schuur et al., 2015; Arctic Monitoring and Assessment Programme, 2021) and is most pronounced in fall and winter (Rantanen et al., 2022). In the Arctic, aerosols and clouds are key components modulating the surface radiation balance and thereby surface temperatures (Shindell and Faluvegi, 2009; Li et al., 2022) but current understanding of processes controlling their distribution, properties, and radiation impacts are associated with large uncertainties (Carslaw et al., 2013, Willis et al., 2018; Schmale et al., 2021). Aerosols can directly affect the radiative budget by absorbing or scattering solar radiation (aerosol-radiation interaction, ARI) or indirectly by impacting cloud formation, lifetime, and radiative properties due to their ability to act as cloud condensation nuclei (CCN) or ice nucleating particles (INPs) (aerosol-cloud interactions, ACI).

While mainly absorbing aerosol can lead to warming of the atmosphere (Li et al., 2022) or reduce the surface albedo upon deposition (Hansen and Nazarenko, 2004; Doherty et al., 2010), scattering particles such as sea salt aerosol (SSaer) and sulfate can induce a cooling effect by reducing the amount of incoming solar radiation at the surface (Charlson et al., 1992; von Salzen et al., 2022), with higher scattering efficiency for accumulation and coarse-mode particles (Seinfeld and Pandis, 2016). Most pan-Arctic stations show absorption and scattering maxima in winter and spring, and a minimum in summer (Schmeisser et al., 2018). Clouds over pack ice in the central Arctic typically exert a net warming effect due to the reemission of absorbed longwave radiation to the surface (Curry et al., 1996), except during a brief period in summer when the reflection of shortwave radiation has a net cooling effect (Shupe and Intrieri, 2004). The timing of the forcing may be a relevant control of the amplitude and timing of sea ice melt (Zhao and Garrett, 2014). In regions with a low baseline aerosol concentration, such as the central Arctic during certain seasons (e.g., fall, winter), cloud longwave emissivity is sensitive to CCN concentrations, and an increase in aerosol number concentrations can amplify longwave emissivity and surface warming (Garrett et al., 2002; Garrett and Zhao, 2006; Mauritsen et al., 2011). The presence of giant CCN can also affect water vapor distribution and precipitation formation (Feingold et al., 1999; Jensen and Nugent, 2017)

but its effects in the Arctic remain largely unknown. Climate models struggle to adequately represent aerosol and cloud radiative effects in the Arctic particularly due to a limited understanding of aerosol sources and properties (Mauritsen et al., 2011; Taylor et al., 2019; Inoue et al., 2021; Wei et al., 2021; Lapere et al., 2023; Solomon et al., 2023).

Arctic aerosol concentrations are governed by a strong seasonality, dependent on varying emission sources and transport processes, atmospheric stability and aerosol removal efficiency (Croft et al., 2016; Willis et al., 2018). During winter and spring, aerosol mass and number concentrations are typically high due to long-range transport from lower latitudes of primarily anthropogenic emissions, which accumulate in the stable atmosphere, also referred to as Arctic haze (Mitchell, 1957; Quinn et al., 2007). Aerosol lifetimes are typically longest during these seasons due to low wet removal efficiencies (Croft et al., 2016). With emission reductions at mid-latitudes particularly between 1990 and 2000, negative trends have been observed on a pan-Arctic scale for typical Arctic haze chemical species, such as sulfate and black carbon (Quinn et al., 2007; Schmale et al., 2022). Summer is characterized by low aerosol mass concentrations and a higher importance of local and regional sources, as long-range transport is reduced due to the contraction of the Arctic dome, and wet scavenging is more efficient (Stohl, 2006; Willis et al., 2018). Aerosol number concentrations are however high in summer, as new particle formation can lead to high abundance of nucleation and Aitken mode particles (Freud et al., 2017; Boyer et al., 2023). Fall typically shows very low aerosol mass and number concentrations with less new particle formation than in summer, limited long-range transport and efficient wet removal (Croft et al., 2016; Freud et al., 2017). Many studies have focused on anthropogenic aerosol sources since they make up the dominant contribution to the aerosol budget in winter and spring, but their decline leads to an emerging interest in better understanding the natural Arctic aerosol baseline, since their climate-relevant properties and source processes remain poorly constrained (Schmale et al., 2021).

SSaer is one of the most abundant natural aerosols globally and is typically produced by wave breaking and bubble bursting over the open ocean (de Leeuw et al., 2011). In polar regions however, SSaer mass concentrations peak in winter (Rankin and Wolff, 2003; Legrand et al., 2016; Schmale et al., 2022) when the ocean is predominantly sea ice covered, and when boundary layer heights are lower and aerosol removal slower. While some of the SSaer can be long-range transported to polar regions from the open ocean and marginal ice zone, the

observed SSaer number concentrations and seasonality cannot solely be explained by climate models with open-ocean emissions (Huang and Jaeglé, 2017; Lapere et al., 2023), which points to sources from the sea ice region, such as open leads, frost flowers, and/or blowing snow. SSaer from open leads has been observed from fall to spring in the coastal Alaskan Arctic (Radke et al., 1976; May et al., 2016; Kirpes et al., 2019; Chen et al., 2022), but this process is unlikely to account solely for SSaer winter-time maxima in the central Arctic pack ice, given mean open-water fractions in Arctic sea ice of the order of 0.1%–1% (von Albedyll et al., 2022; Lapere et al., 2024; von Albedyll et al., 2024). Saline frost flowers have also been hypothesized as a sea ice SSaer source (Rankin et al., 2000; Rankin et al., 2002; Kaleschke et al., 2004), given the depleted sulfate signature in Antarctic SSaer that is similar to brine and frost flowers (Wagenbach et al., 1998), but laboratory experiments have shown low emission efficiencies (Roscoe et al., 2011; Yang et al., 2017). Modeling experiments indicate a minor importance of frost flower SSaer emissions, but propose sublimating salty blowing snow as an important source (Yang et al., 2008; Huang and Jaeglé, 2017; Confer et al., 2023; Lapere et al., 2023), recently confirmed by observations in the Antarctic (Giordano et al., 2018; Frey et al., 2020). Including a blowing snow SSaer source in numerical models results in better agreement with measurements (Huang and Jaeglé, 2017; Yang et al., 2019; Ranjithkumar et al., 2025). According to current process understanding, saline snow can result from upward brine migration into the snowpack, SSaer deposition from leads or the open ocean (Domine et al., 2004; Peterson et al., 2019), or salty, ocean-sourced "snow" formed from sublimating sea ice (Macfarlane et al., 2023a), with multiple processes contributing depending on snow depth. When blowing snow occurs under high wind speed, the sublimation of salty snow particles in subsaturated air is thought to leave behind SSaer of which the concentrations and size are thought to depend primarily on snow salinity and snow particle size (Yang et al., 2019).

Most of our understanding of Arctic SSaer sources and blowing snow aerosols are based on modeling studies (Yang et al., 2008; Huang and Jaeglé, 2017; Rhodes et al., 2017; Yang et al., 2019; Lapere et al., 2024) with only few direct observational studies. SSaer emissions have been linked to blowing snow in Antarctica (Giordano et al., 2018; Frey et al., 2020), where Frey et al. (2020) show the first direct observations of SSaer from blowing snow above sea ice from a cruise in the Weddell sea with 200–1,000 km distance to the open ocean. SSaer concentrations increased during and after storms, and similar depletion in sulfate relative to sodium with respect to sea water in bulk aerosol and snow on sea ice, show evidence of a sea ice source. Near Utqiaġvik, Chen et al. (2022) observed blowing snow to be over-predicted by the current parameterization and measured the composition of single particle fresh SSaer during blowing snow to be consistent with sea spray aerosol emissions from local open leads, with supermicron aerosol suggested to be scavenged by the blowing snow. Gong et al. (2023)

show strong increases in fine-mode aerosol and CCN concentrations with blowing snow during the Multidisciplinary drifting Observatory for the Study of Arctic Climate (MOSAiC) and estimated increased longwave emission of $+2.3$ W m$^{-2}$ resulting in surface warming, underlining the potential climate-relevance of blowing snow SSaer. Ranjithkumar et al. (2025) show that a large fraction of coarse aerosol (0.5–20.0 µm) concentrations observed at 2 m above the sea ice from November 2019 to mid-May 2020 can be explained by sea salt originating from salty blowing snow that undergoes sublimation. The authors employed the chemistry transport model p-TOMCAT to simulate total coarse-mode sea salt concentrations (e.g., Yang et al., 2019) with and without blowing snow, and improved the correlation with observations of total aerosol using an updated blowing snow parameterization, which considers variable wind speed and snow salinity.

Despite these advances, many open questions regarding Arctic wind-sourced aerosol remain. In this study, we address the following questions: What are the aerosol characteristics during blowing snow events (BSEs) in the central Arctic, and which environmental parameters influence blowing snow and wind-sourced aerosol concentrations? What are the impacts of high wind speed and BSEs on aerosol size distributions, CCN, INPs, and optical properties, as a function of season, in particular in fall to spring? When and where in the Arctic could wind-sourced aerosol play a role for radiation and cloud interactions?

To address these questions, we investigate year-long observations during the MOSAiC drift experiment in the central Arctic ocean from 2019 to 2020. Specifically, we characterize wind-sourced aerosol during BSEs including a case study and an overview of BSE characteristics of aerosol properties and environmental conditions from fall to spring. We further assess the aerosol size distributions, scattering coefficients, submicron NaCl levels, and abundance of CCN and INPs dependent on wind speed and season. Finally, we discuss possible spatio-temporal climate impacts and comment on the use of the data and findings for model evaluation.

## 2. Methods
### 2.1. MOSAiC expedition
This study is based on observations collected during the MOSAiC expedition, which was designed to study the changing Arctic climate system and the coupled atmospheric, sea ice, ocean, and ecosystem processes. The purpose of the expedition was to address knowledge gaps of the central Arctic climate system and aims to improve modeling capabilities through the wealth of data collected over a full seasonal cycle, particularly during winter when previous observations are most lacking. The German Research Vessel (RV) *Polarstern* (Knust, 2017) was frozen into the sea ice north of the Laptev Sea in October 2019, and drifted across the Arctic Ocean following the Transpolar Drift route, trapped in the ice for most of the time until September 2020. Freeze up occurred in 2019 before the expedition started and the melt onset in late May

2020 (Itkin et al., 2023). Overviews of the drift track and measurements regarding the atmosphere, snow and sea ice, and oceanography can be found in Shupe et al. (2022), Nicolaus et al. (2022), and Rabe et al. (2022), respectively. The diverse and interdisciplinary measurements in the central Arctic make this dataset well suited to investigate wind-sourced aerosol including potential controlling environmental factors. The different variables used in this study are described in the following sections and summarized in Table S1.

### 2.2. Aerosol-related data

#### 2.2.1. Aerosol concentrations and size distributions
In this study, we focus on coarse-mode aerosol (>1 μm aerodynamic diameter $d_a$) but consider aerosol sizes between 20 nm (electrical mobility diameter $d_m$) and 16 μm ($d_a$). Coarse-mode aerosol size distributions were measured with an Aerodynamic Particle Sizer (APS model 3321, TSI Inc., USA) in the *Swiss* container on the P-deck of RV *Polarstern* (overview of the ship in Shupe et al., 2022) with an inlet height of 15 m above sea level. The original APS diameters were adjusted based on experiments with polystyrene latex spheres, and a correction factor was applied per bin based on comparison with the Wideband Integrated Bioaerosol Sensor—New Electronics Option (WIBS NEO; Droplet Measurement Technologies, Longmont, CO, USA), located on the same inlet (Beck et al., 2024). This results in a particle range from 1.06 to 16.1 μm ($d_a$), and details of the comparison, correction, and inlet systems are described in Heutte et al. (2023). In this study, we refer to total concentrations from the APS as coarse-mode aerosol concentration. Size distributions from the Ultra-High-Sensitivity Aerosol Spectrometer (UHSAS, Droplet Measurement Technologies Inc., USA) were used for fine-mode particles (60–1,000 nm optical diameter $d_{opt}$) and measured in the Atmospheric Radiation Measurement (ARM) Aerosol Observing System (AOS) container (Uin et al., 2019) adjacent to the *Swiss* container. To obtain merged particle number size distributions with a diameter range from 60 nm to 8 μm ($d_{opt}$), the UHSAS and APS size distributions were merged by applying a weighted average in the overlapping size bins (linear weights decreasing to size distribution limits). We also use data from the Scanning Mobility Particle Sizer (SMPS model 3936; TSI Inc., USA), which measured size distributions between 10 and 500 nm ($d_m$, Boyer et al., 2023) and which was also located in the AOS container.

#### 2.2.2. Submicron particulate NaCl
Submicron NaCl levels were estimated from an Aerodyne high-resolution time of flight mass spectrometer (HR-ToF-AMS, referred to as AMS), for which the operation and post-processing for MOSAiC is described in Heutte et al. (2023). NaCl, a refractory species, cannot be quantitatively detected by the AMS, but can be measured in combination with non-refractory species (Salcedo et al., 2006). NaCl mass concentrations were estimated using the AMS $^{23}$Na$^{35}$Cl$^+$ signal multiplied by 51, following an approach of Ovadnevaite et al. (2012). Since the calibration factor of the AMS used in Ovadnevaite et al. (2012) is unlikely to be

identical to the AMS used during MOSAiC, our NaCl signals are provided in arbitrary units (a.u.), as in Heutte et al. (2025). We only assess submicron NaCl in fall and spring as the AMS was not operational in winter (December–February).

#### 2.2.3. CCN concentration and hygroscopicity parameter kappa
CCN were measured in the ARM container on RV *Polarstern* using a Cloud Condensation Nuclei Counter (CCNC, model CCN-100, Droplet Measurement Technologies, Boulder, CO, USA) (Roberts and Nenes, 2005). Supersaturations were varied in hourly cycles from 0.12%, 0.27%, 0.54% to 0.76%, where we use CCN concentrations for a supersaturation of 0.27% (which we refer to as 0.3%) averaged by the mean to 10 min resolution in this study. Supersaturations of 0.3% are relevant in the Arctic (Motos et al., 2023). The bulk hygroscopicity parameter, kappa ($\kappa$), is calculated following Petters and Kreidenweis (2007):

$$\kappa = \frac{4\,A^3}{27\,D_{crit}^3 \ln^2 S_c}$$

where $S_c$ is the critical supersaturation ratio, $A$ is defined as $A = \frac{4\,\sigma_{\frac{a}{w}}\,M_w}{R\,T\,\rho_w}$ with the surface tension of water in air $\sigma_{\frac{a}{w}} = 0.072$ J m$^{-2}$, temperature $T = 298.15$ K, the density of liquid water $\rho_w = 997$ kg m$^{-3}$, the molar mass of water $M_w = 18.015 \times 10^{-3}$ kg mol$^{-1}$, and the gas constant $R = 8.3145$ J mol$^{-1}$ K$^{-1}$. $D_{crit}$ is derived from integrating SMPS number concentrations from the largest size bin and choosing the diameter where integrated concentrations match closest to CCN number concentrations at a given supersaturation. As for CCN concentrations, we use the hygroscopicity parameter at 0.3% supersaturation.

#### 2.2.4. INP measurements
Immersion-mode INP measurements were performed on the Colorado State University cold plate from daily integrated aerosol samples collected with the 4-stage Davis Rotating-drum Unit for Monitoring cascading impactor (DRUM model DA-400; DRUMAir$^{TM}$) at an average flow of 31.6 L min$^{-1}$. In this study, we only show the total INP concentrations (0.15 to > 12 μm $d_a$) at $-20°$C. INPs at $-20°$C were detected year-round, whereas INPs at warmer temperatures were only present in summer (Creamean et al., 2022). A more detailed description of the sampling and measurement set-up can be found in Creamean et al. (2022).

#### 2.2.5. Aerosol optical data
A nephelometer (TSI model 356) located in the AOS container was used to measure total aerosol light scattering coefficients at 3 wavelengths (blue—450 nm, green—550 nm, and red—700 nm) in 1 min time resolution. Scattering coefficients were measured alternately for aerosol particle sizes <10 μm and <1 μm ($d_a$), by having an impactor assembly on the nephelometer sampling line that automatically switched between 1 μm and 10 μm size cuts (Uin et al., 2019). We used the green wavelength

for both scattering coefficient measurements in this study and averaged them to 10 min time resolution using the mean. If not directly indicated, the scattering coefficient for aerosol size <10 μm is used. For scattering coefficients for aerosol particles in the 1–10 μm size range, we linearly interpolate both scattering coefficient measurements in time and subtract the coefficients for <1 μm from those measured at <10 μm.

The Scattering Ångström exponent (SAE) is calculated with

$$\text{SAE} = \frac{\log(\sigma_{sp\ 450\ nm}/\sigma_{sp\ 550\ nm})}{\log(\lambda_{450\ nm}/\lambda_{550\ nm})}$$

and describes how the scattering coefficient $\sigma_{sp}$, depends on wavelength $\lambda$, using the green and blue wavelengths. Aerosol absorption coefficients, $\sigma_{ap}$, were also measured in the AOS container by a 3 wavelength Particle Soot Absorption Photometer including the impactor assembly described above, alternately sampling aerosol at <10 μm and <1 μm ($d_a$). The absorption coefficients used in this study are for the green wavelength and particles <10 μm. The single scattering albedo ($\omega$) is calculated with

$$\omega = \frac{\sigma_{sp\ 550}}{\sigma_{sp\ 550} + \sigma_{ap\ 550}}$$

and indicates the relative light scattering versus light extinction of the aerosol population.

### 2.2.6. Influence of local pollution
Aerosol measurements during MOSAiC were often influenced by local research activities and stack emissions from RV *Polarstern* (Beck et al., 2022). The local pollution influence needs to be filtered out to analyze ambient aerosol concentrations. As coarse-mode aerosol concentrations are less influenced by ship pollution, for which the size distribution peaks at around 30 nm, a pollution detection algorithm by Beck et al. (2021) was applied to the total coarse-mode concentration (Heutte et al., 2023). For measurements that are more strongly influenced by local fresh pollution including the UHSAS, SMPS, and optical data, a stricter pollution mask based on condensation particle counter measurements was used (Heutte et al., 2023). For the AMS, a cosine similarity approach described by Dada et al. (2022) was used to remove fresh pollution (Heutte et al., 2023). The percentage of removed data is included in Table S1.

### 2.3. Ancillary data
#### 2.3.1. Meteorological data
In this study, we use 10 m wind speed measured with a Metek u-Sonic3 Cage MP on a tower, which was located on the sea ice approximately 500 m from RV *Polarstern* (Cox et al., 2023). Time gaps were filled by calculating 10 m wind speeds from wind speed measurements at 39 m height on RV *Polarstern* (Schmithüsen, 2021a, 2021b, 2021c, 2021d, 2021e) assuming a neutral logarithmic wind speed profile and a roughness length of $z_0 = 5.6 \cdot 10^{-3}$ m (Cox et al., 2023). Given that other wind speed data are also used in this study (trajectory and ERA5 wind

speed as described in Section 2.3.4), we refer to the local wind speed measurements as in situ wind speed. Temperature and relative humidity with respect to liquid water ($RH_w$) were also measured at 10 m on the tower with a Vaisala PTU307. $RH_w$ was converted into relative humidity with respect to ice ($RH_{ice}$) following Hyland and Wexler (1983) and Cox et al. (2023). Liquid equivalent snowfall rates at approximately 170 m height were retrieved based on Ka-band (approximately 35 GHz) zenith-pointing radar (KAZR) measurements by Matrosov (2024). Atmospheric boundary layer (ABL) heights were retrieved from balloon-borne Vaisala RS41 radiosondes every 6 hours based on a bulk Richardson number-based approach (Jozef et al., 2023b).

#### 2.3.2. Snowdrift density
An open-path Snow Particle Counter (SPC-95, Niigata Electric Co., Nishimura and Nemoto, 2005; Nishimura et al., 2014) measured the size distribution of airborne snow particles (36–490 μm) at 0.1 and 10 m above the surface at the wind speed measurement tower on the sea ice (Ranjithkumar et al., 2025). The snow particle size distributions were used to compute snowdrift density. We mostly show the drift density from the lower SPC, except in November where only data from the upper SPC are available.

#### 2.3.3. Snow properties
Snow salinity was measured approximately weekly from snow pit profiles at multiple depths. The samples taken with a snow density cutter of 100 cm³ volume were melted and analyzed for practical salinity in ppt (parts per thousand for mass) using a YSI 30 Salinity, Conductivity, and Temperature sensor in the laboratory on RV *Polarstern*. Snow hardness shown in Figure S6 indicates the median of the uppermost 3 cm of snow force profiles measured with a snow micro penetrometer. More details on measurement methods and locations can be found in Macfarlane et al. (2023b).

#### 2.3.4. ERA5 wind speed frequency and trajectory wind speed
Frequency of wind speeds >9 m s$^{-1}$ (high wind speed threshold where aerosol concentrations are increased, Section 3.3) was calculated for each month based on hourly ERA5 (Hersbach et al., 2020) 10 m wind speed north of 60°N with a horizontal resolution of 0.25° for the years 2010–2020. Mean wind speed for trajectories arriving at RV *Polarstern* were computed from 3-hourly displacement of kinematic back-trajectories calculated using the Reading Offline Trajectory Model (ROTRAJ) (Methven et al., 2003). Large-scale velocity fields at the Lagrangian particle positions are obtained from 3-hourly ERA5 reanalysis data at a resolution of approximately 0.7°, using cubic Lagrange interpolation in the vertical, followed by bilinear interpolation in the horizontal, and linear interpolation in time. Time periods with unphysical oscillations that could be due to model artifacts were removed from the analysis. Comparing the trajectory wind speed of time lag 0 at the location of RV *Polarstern* (at an altitude just above the

surface, 99% of surface pressure) with the in situ measured wind speed at 10 m shows good agreement in magnitude (difference in mean wind speeds approximately 10%) and high correlation ($r_{spearman} = 0.94$, $P < 0.001$; we mainly use Spearman's rank correlation coefficient throughout the manuscript as it is less sensitive to outliers and nonlinearity, and a significance level of 0.05).

### 2.3.5. Ground-based remote sensing

The 910 nm backscatter coefficients were measured by the Vaisala CL31 ceilometer single backscatter lidar system on the P-deck of RV *Polarstern*. The 532 nm backscatter coefficient and lidar ratio are used from multiwavelength polarization Raman lidar Polly (POrtabLe Lidar sYstem, Engelmann et al., 2016) measurements, which were performed in the OCEANET-Atmosphere container near the *Swiss* container.

### 2.3.6. Sea ice extent

For a monthly overview of wind speed frequency over sea ice, we use monthly averaged Arctic sea ice extent for the MOSAiC campaign from the Sea Ice Index version 3 product with a spatial resolution of 25 km × 25 km (Fetterer et al., 2017), provided by the National Snow and Ice Data Center (NSIDC). The product is derived from 2 passive microwave-derived datasets (Near-Real-Time SMPS SSMIS Daily Polar Gridded Sea Ice Concentrations and the Sea Ice Concentrations from Nimbus-7 SMMR and DMSP SSM/I-SSMIS Passive Microwave Data) and monthly sea ice extent is based on when the grid cell's sea ice concentration average is above 15%.

### 2.4. Blowing snow event definition

We base our definition of BSEs on Gong et al. (2023), where blowing snow periods are identified when the snow drift density at 0.1 m above ground exceeds $10 \times 10^{-5}$ kg m$^{-3}$ and 10 m wind speeds are higher than the critical wind speed of blowing snow initiation based on the empirical model by Li and Pomeroy (1997), which is temperature dependent. Since aerosol concentrations typically peak and decay with a delay to blowing snow (Frey et al., 2020), we extend the event duration by visual inspection of the coarse-mode aerosol concentration and the time they return to their baseline. Start and end times of BSEs can be found in Table S2. Since in November 2019, snow-drift density data are missing at 0.1 m, Gong et al (2023) included the condition of snowdrift density at 10 m and increased aerosol mass concentrations, which is also applied here. Even though the initial event definition is based on blowing snow, aerosol particles during BSEs can also originate from other wind-driven sources such as open leads, or be long-range transported and include SSaer from the open ocean, or other aerosol sources (e.g., anthropogenic emissions). We therefore often use the more general term wind-sourced aerosol.

### 2.5. Blowing snow height estimates

Blowing snow height estimates are based on ceilometer backscatter coefficients following a similar procedure as described in Gossart et al. (2017) and Loeb and Kennedy

(2021). From the lowest usable bin (bin 5 at 45 m), the algorithm checks whether the backscatter is higher than the clear sky threshold, which was set to $25 \times 10^{-4}$ km$^{-1}$ sr$^{-1}$, the 99th percentile of bin 5 backscatter values of clear sky time periods that were selected by visual inspection of daily ceilometer backscatter figures. It is similar to the clear sky threshold reported in Gossart et al. (2017) and Loeb and Kennedy (2021). The algorithm then checks whether the backscatter is decreasing by testing whether the bin 5 backscatter coefficient is larger than the average backscatter coefficient of bins 6–8. If this condition is fulfilled, the blowing snow height is set to the height of the last bin that shows higher backscatter values than the clear-sky threshold, or in case of precipitation, the height of the bin where backscatter values increase again. During precipitation, blowing snow height estimates sometimes show repeatedly the same values due to the high back-scatter signal. Blowing snow starts to occur in shallow drift layers close to the surface, which may not be detected by the ceilometer. Therefore, we only assess blowing snow height estimates in case studies when we know BSEs are occurring, and in precipitation free periods (identified by the ceilometer backscatter data). Therefore, we do not need to assess false positives, that is, blowing snow detection based on ceilometer profiles when no blowing snow was observed.

## 3. Results and discussion

We present and discuss the results of our study in the following structure: First, we provide a case study example of a BSE to illustrate how properties are derived, followed by a general overview of BSEs and their dependence on wind speed. Next, we present a seasonal overview of coarse-mode aerosols and BSEs, followed by an analysis of the wind's influence on aerosol properties, including size distributions, optical properties, submicron NaCl, and CCN and INP budgets. We conclude this section with an Arctic-wide discussion of the climate effects of wind-sourced aerosols, considering seasonal variations.

### 3.1. Blowing snow event —Case study November 10–12, 2019

The BSE from November 10–12, 2019 (**Figure 1**, all time information provided in UTC) shows a typical evolution of BSEs during MOSAiC. With increasing wind speed on November 11, blowing snow emerges as seen in the drift density enhancement. Aerosol number concentration also rises and peaks with approximately 3.5 h delay compared to the in situ wind speed maximum (**Figure 1a**), with the delayed peak being a common feature of many BSEs and typically in the order of a few hours (Figure S1) (Frey et al., 2020). The snowfall and snowdrift maxima concurrent to the wind speed maximum on November 11 afternoon may scavenge some of the aerosol particles, contributing to the delayed aerosol concentration increase (Frey et al., 2020; Chen et al., 2022). Additionally, the decreased presence of airborne snow particles near the surface and the RH$_{ice}$ (at 10 m) decrease to below 100% (**Figure 1b**) likely drive increased snow particle sublimation and therefore maximum aerosol concentrations observed at this time
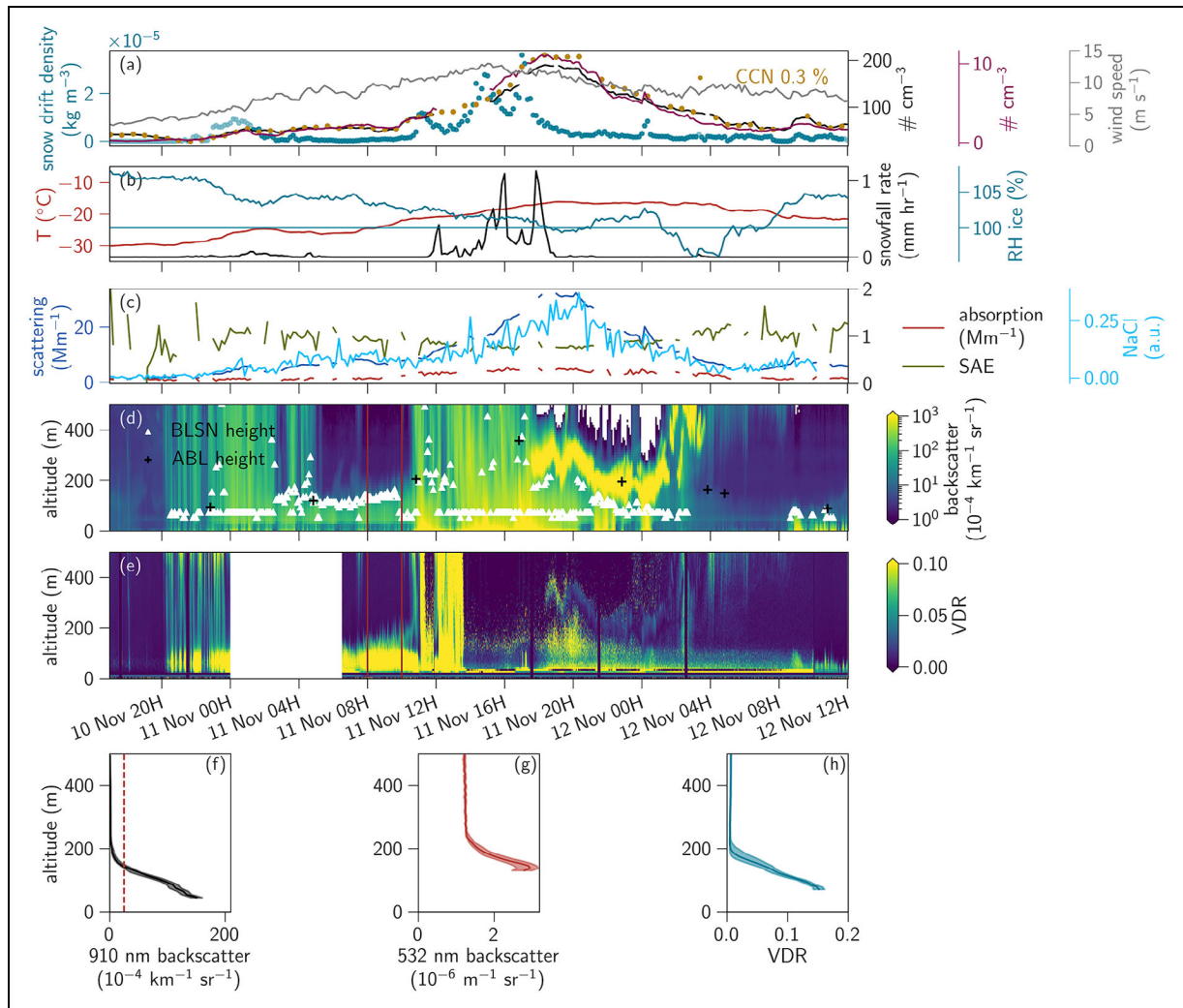
**Figure 1. November blowing snow case study.** Time series (in UTC) with (a) the snow drift density at 10 m, total number concentrations from the merged size distribution (0.06–8 µm $d_{opt}$) in black, cloud condensation nuclei (CCN) at 0.3% supersaturation in yellow (first right axis), and coarse-mode (1.06–16.1 µm $d_a$) in magenta (inlet height 15 m), in situ wind speed, and (b) temperature, relative humidity with respect to ice ($RH_{ice}$) at 10 m and snowfall rate at 170 m, (c) the scattering coefficient, the absorption coefficient, and Scattering Angström exponent (SAE) (right $y$-axis), all for particles up to 10 µm with an inlet height around 18 m, and the submicron NaCl signals ($\times 51$). (d) Ceilometer 910 nm total backscatter including blowing snow height estimates (BLSN height, white triangles) and atmospheric boundary layer height (ABL height, black crosses) and (e) Polly volume depolarization ratio (VDR). Atmospheric profiles of time subset from November 11, 08:00 to 10:00 UTC (marked with red vertical lines in d and e) of (f) median and interquartile range ceilometer backscatter, (g) Polly 532 nm backscatter, (h) Polly VDR. The red dashed line in (f) marks the clear-sky threshold.

(11 Nov 18:00). For this event, in situ wind speed (at 10 m) and coarse-mode aerosol concentration (at 15 m) correlate significantly ($r_{spearman} = 0.86$, $P < 0.001$), and correlation is even higher ($r_{spearman} = 0.89$, $P < 0.001$) when accounting for the time lag of 3.5 h. The total particle number of the merged size distribution (0.06–1 µm $d_{opt}$), the coarse-mode aerosol number concentrations (1.06–16 µm $d_a$) and the CCN concentrations follow each other closely, suggesting a common source process across the whole size range, likely blowing snow sublimation in this case. Open leads could also contribute to enhanced aerosol concentrations but were likely less important during this event with lead fractions <1% in a 50 km radius around RV *Polarstern* (Heutte et al., 2025), which is likely representative for the larger surrounding since lead fractions were similar on larger spatial scales and regions (Krumpen et al., 2021; von Albedyll et al., 2024). In fact, some BSEs show a different evolution of fine and coarse-mode aerosol number concentrations which are likely explained by the co-occurrence of locally generated (blowing snow sublimation and/or emission from leads) and long-range transported aerosol (e.g., anthropogenic pollution), which is discussed in more detail in Heutte et al. (2025). Temperatures during the event range from $-30°C$ to $-17°C$ with $RH_{ice}$ around saturation with super- and subsaturated periods. Given the increased aerosol concentrations and uncertainties of the RH measurement (approximately 5%), we would expect snow crystal sublimation to take

place throughout the event. The scattering coefficient closely follows the total aerosol concentrations while the absorption coefficient stays at near zero values and the SAE shows slightly lower values indicating primarily scattering aerosols are present, consistent with coarse-mode aerosol and NaCl (**Figure 1c**). In some cases (e.g., Figure S2), also the absorption coefficient increases during the event, which could be due to the concurrent transport of absorbing aerosol, and/or reemission of previously deposited absorbing aerosol (Heutte et al., 2025). Overall, this November 2019 case study shows similar characteristics in terms of meteorology and aerosol properties as described by Frey et al. (2020) for the Southern Ocean and for other MOSAiC events (Gong et al., 2023; Ranjithkumar et al., 2025).

To assess if BSEs and wind-sourced aerosol can have an impact on or interact with clouds, we examine the vertical extent using ceilometer and lidar data. Concurrent with elevated in situ wind speed and snow drift density, the ceilometer backscatter is enhanced close to the surface from November 10 evening to November 12 morning (**Figure 1d**). Time periods with snowfall show increased backscatter throughout the column as well as the presence of a low-level, likely mixed-phase cloud from November 11 afternoon to November 12 morning. Blowing snow height estimates are more reliably interpretable without precipitation, such as on November 11 from 08:00 to 10:00 (between the red lines, **Figure 1d, e**). The vertical extent of blowing snow during this time reaches 135 m (median, 125–145 m interquartile range, IQR). The enhanced volume depolarization ratio (VDR, **Figure 1e**) of the Polly lidar (Engelmann et al., 2016; Engelmann et al., 2021) shows a similar temporal evolution and vertical extent as the ceilometer backscatter, supporting the assumption that the signal comes from blowing snow as higher values indicate nonspherical particles such as ice crystals. The high in situ wind speed makes other sources of near surface ice crystals, such as diamond dust (which forms under calm conditions), unlikely that could generate the same VDR and backscatter signals. The profiles of the ceilometer backscatter (**Figure 1f**), the Polly backscatter (**Figure 1g**), and the Polly VDR (**Figure 1h**) show enhanced values up to a similar height range, decreasing to a constant value at approximately 200 m. The cloud base height from November 11 afternoon to November 12 morning lies above the estimated blowing snow height (approximately 145–370 m based on ceilometer cloud base heights) but is similar to the atmospheric boundary layer height (195–375 m). On November 11, 22:53, the atmospheric boundary layer height was 195 m with a ceilometer cloud base height of 198 m at the same time. The temperature profile is relatively constant up to 200 m with an inversion above (Figure S3), indicating well-mixed conditions and suggesting that the cloud could be coupled to the surface. In this case, snow crystal residues, that is, aerosol particles, could be present above the blowing snow height and within the entire boundary layer, potentially influencing the cloud in this case.

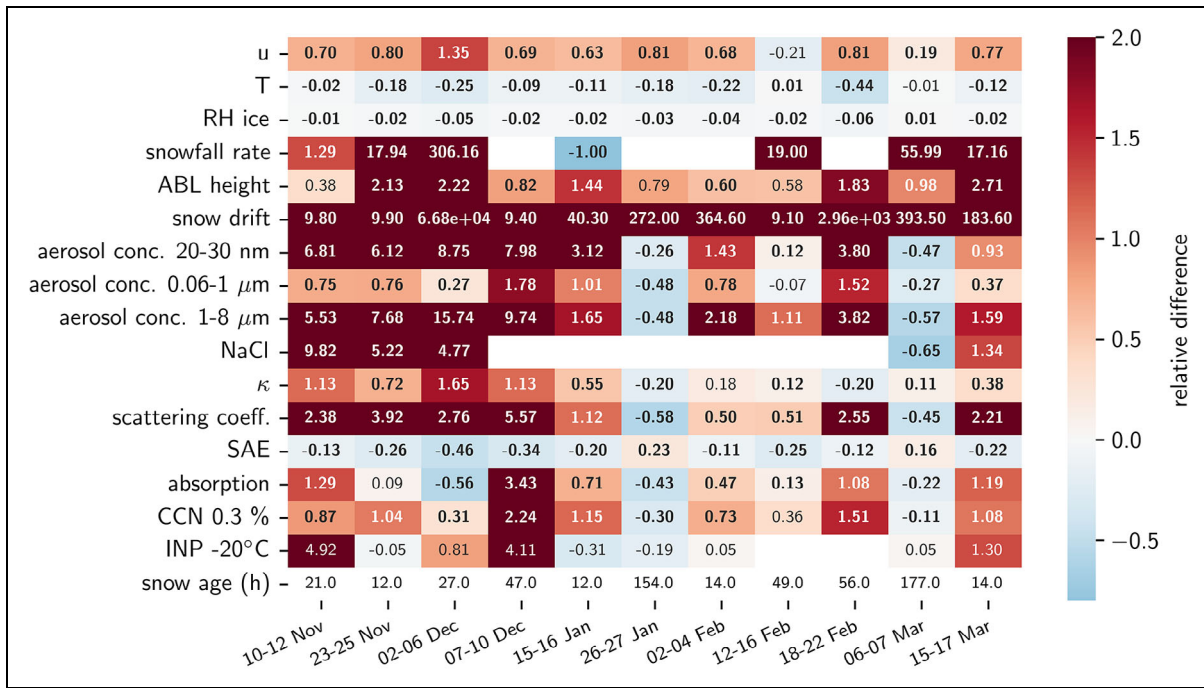Including the specific BSEs shown in the supplementary information (Figures S2, S4, Section S2), the 3 different BSE case studies show median blowing snow altitudes of 135 m (125–145 m IQR), 145 m (125–155 m IQR), and 95 m (85–155 m IQR), respectively (55–195 m minimum and maximum in the considered time periods for all three events), with similar VDR profiles (change in gradient between approximately 145–195 m, therefore a bit higher than the blowing snow heights but for VDR and backscatter, no clear sky threshold was defined). The aerosol residues from blowing snow are expected to reach at least as high as the blowing snow layer, but could likely be present throughout the boundary layer in well-mixed stormy periods (Jozef et al., 2023a), and thus, in the lower hundreds of meters in the atmosphere where low-level clouds can also be present. During MOSAiC, 16% of the cloud base heights from November to April were below 200 m and 25% below 300 m (not shown), therefore within the altitude range of possible blowing snow aerosol influence.

### 3.2. Blowing snow event overview

In total, we identified 29 BSEs between November 2019 and May 2020 (Table S2), and **Figure 2** provides an overview of the subset of 11 BSEs that were predominantly unpolluted from RV *Polarstern* ship stack emissions (Section 2.2.6). The overview matrix shows the relative difference of the variable median during the event from the baseline (difference of BSE and baseline divided by the baseline). The baseline is defined as the median of the variable in the time period including the 15 days before and after the event, excluding the BSE itself and potential adjacent BSEs. For the environmental variables, by definition, BSEs typically show enhanced wind speed and snow drift density compared to the baseline. ABL heights are increased during events, which is related to increased turbulence and mechanical mixing during stormy periods (Peng et al., 2023), leading to near neutral or weakly stable boundary layer regimes during MOSAiC storms (Jozef et al., 2023a). During all events, some snowfall occurs with the majority of events showing an enhanced snowfall rate compared to the baseline time period. Temperature and relative humidity only change very little, but are typically lower during the events.

For the aerosol observations, the majority of events had an increase in sub- and supermicron aerosol number concentrations during BSEs. The enhancements are higher for supermicron aerosol (relative differences between −0.57 and 15.74) and ultrafine aerosol (20–30 nm $d_m$, relative differences between −0.47 and 7.98) than for submicron aerosol (relative differences between −0.48 and 1.78), which is further discussed in Section 3.4. The pattern of aerosol properties during BSEs is mostly explained by the relationship of these variables to each other: BSEs are expected to enhance mostly SSaer which is observed when NaCl data are available; it is a scattering aerosol which agrees with an increase in the scattering coefficient. Sea salt is also a hygroscopic aerosol and a good CCN, in line with higher $\kappa$ values and increased CCN concentrations during the events, as also observed by Gong et al. (2023). The stronger relative enhancement of supermicron aerosol also shows in the reduction of the SAE during BSEs. The relative enhancements are approximately

| | 10-12 Nov | 23-25 Nov | 02-06 Dec | 07-10 Dec | 15-16 Jan | 26-27 Jan | 02-04 Feb | 12-16 Feb | 18-22 Feb | 06-07 Mar | 15-17 Mar |
|---|---|---|---|---|---|---|---|---|---|---|---|
| u | 0.70 | 0.80 | 1.35 | 0.69 | 0.63 | 0.81 | 0.68 | -0.21 | 0.81 | 0.19 | 0.77 |
| T | -0.02 | -0.18 | -0.25 | -0.09 | -0.11 | -0.18 | -0.22 | 0.01 | -0.44 | -0.01 | -0.12 |
| RH ice | -0.01 | -0.02 | -0.05 | -0.02 | -0.02 | -0.03 | -0.04 | -0.02 | -0.06 | 0.01 | -0.02 |
| snowfall rate | 1.29 | 17.94 | 306.16 | | -1.00 | | | | 19.00 | 55.99 | 17.16 |
| ABL height | 0.38 | 2.13 | 2.22 | 0.82 | 1.44 | 0.79 | 0.60 | 0.58 | 1.83 | 0.98 | 2.71 |
| snow drift | 9.80 | 9.90 | 6.68e+04 | 9.40 | 40.30 | 272.00 | 364.60 | 9.10 | 2.96e+03 | 393.50 | 183.60 |
| aerosol conc. 20-30 nm | 6.81 | 6.12 | 8.75 | 7.98 | 3.12 | -0.26 | 1.43 | 0.12 | 3.80 | -0.47 | 0.93 |
| aerosol conc. 0.06-1 μm | 0.75 | 0.76 | 0.27 | 1.78 | 1.01 | -0.48 | 0.78 | -0.07 | 1.52 | -0.27 | 0.37 |
| aerosol conc. 1-8 μm | 5.53 | 7.68 | 15.74 | 9.74 | 1.65 | -0.48 | 2.18 | 1.11 | 3.82 | -0.57 | 1.59 |
| NaCl | 9.82 | 5.22 | 4.77 | | | | | | | -0.65 | 1.34 |
| $\kappa$ | 1.13 | 0.72 | 1.65 | 1.13 | 0.55 | -0.20 | 0.18 | 0.12 | -0.20 | 0.11 | 0.38 |
| scattering coeff. | 2.38 | 3.92 | 2.76 | 5.57 | 1.12 | -0.58 | 0.50 | 0.51 | 2.55 | -0.45 | 2.21 |
| SAE | -0.13 | -0.26 | -0.46 | -0.34 | -0.20 | 0.23 | -0.11 | -0.25 | -0.12 | 0.16 | -0.22 |
| absorption | 1.29 | 0.09 | -0.56 | 3.43 | 0.71 | -0.43 | 0.47 | 0.13 | 1.08 | -0.22 | 1.19 |
| CCN 0.3 % | 0.87 | 1.04 | 0.31 | 2.24 | 1.15 | -0.30 | 0.73 | 0.36 | 1.51 | -0.11 | 1.08 |
| INP -20°C | 4.92 | -0.05 | 0.81 | 4.11 | -0.31 | -0.19 | 0.05 | | | 0.05 | 1.30 |
| snow age (h) | 21.0 | 12.0 | 27.0 | 47.0 | 12.0 | 154.0 | 14.0 | 49.0 | 56.0 | 177.0 | 14.0 |

(relative difference scale: -0.5 to 2.0)

**Figure 2. Characterization of blowing snow events (BSEs).** Overview of the relative difference between BSE (median of variable during event) compared to the baseline (median of variable during event ± 15 days excluding BSEs) calculated by (BSE − baseline)/baseline for wind speed ($u$), air temperature ($T$), relative humidity with respect to ice (RH$_{ice}$), snowfall rate, boundary layer height (ABL height), snow drift density (snow drift), aerosol concentration in different size ranges (20–30 nm $d_m$, 0.06–1 μm, 1–8 μm $d_{opt}$), submicron NaCl, the hygroscopicity parameter $\kappa$ at 0.3% supersaturation, the scattering coefficient, the scattering Angström exponent (SAE), cloud condensation nuclei (CCN) concentrations at 0.3% supersaturation, and ice nucleating particle (INP) concentrations at −20°C. Red colors indicate an enhancement of the respective variable during BSEs, blue colors a reduction. Bold cell numbers indicate a statistically significant ($P < 0.05$) relative difference between the BSE and baseline distributions based on a Mann-Whitney $U$ test. Snow age (in h) indicates the time since the last snowfall >0.05 mm h$^{-1}$ 12 h before the event start. Measurement heights of the different variables are provided in Table S1.

proportional to each other, with positive correlation coefficients of enhancement of aerosol, NaCl, CCN, scattering, and $\kappa$, and a negative correlation coefficient of SAE enhancement with these variables (shown in the correlation matrix in Figure S5). The stronger enhancements of aerosol number concentrations, CCN, and the scattering coefficient for the BSEs in November and December compared to January through March events could stem from higher NaCl enhancement in fall. This could for example be reflected in higher hygroscopicity enhancements in the November and December BSEs ($\kappa$ relative difference between 0.55 and 1.65) compared to the remaining months ($\kappa$ relative difference < 0.38). The seasonally differing increase in NaCl concentration is further discussed in Section 3.4.3.

Some variables show more inter-event relative differences, such as the absorption coefficient and INP concentrations, which are sometimes elevated or reduced. Absorption coefficient increases could be due to long-range pollution transport and reemission of deposited aerosol (Heutte et al., 2025) and are likely due to submicron aerosol, given the positive correlation of submicron aerosol and absorption coefficient changes (Figure S5). INP concentrations are not systematically increased but could be enhanced due to sporadic long-range transport

of for example, mineral dust (Creamean et al., 2022), or reemission of previously deposited aerosol.

Some events, primarily January 26–27 and March 6–7, deviate from the dominant pattern, and despite enhanced wind speed and snow drift density, median aerosol concentrations and related aerosol properties are reduced compared to the baseline. What these events have in common is a prolonged time period without snowfall before the event (**Figure 2**, Figure S6), >6 days for the January 26–27, case, and >7 days for the March 6–7, but <3 days for all other BSEs. Snow metamorphism typically increases snow bonding which leads to increased resistance to wind transport (Li and Pomeroy, 1997), and the snow surface shows a tendency to be harder with higher snow age (Figure S6b). In addition, wind packing and wind crust formation could also limit blowing snow. However, both events show snow drift density which probably comes from the freshly fallen snow during the event time period. Possibly, fresh dry snow with low salinity is directly lifted, with little contact and mixing with older, more saline snow. The 2 events with lowest snow age before the event show more than double the median aerosol concentrations compared to the 2 events with highest snow age. Yet, no significant correlation between snow age and aerosol concentration can be observed (Figure S5, Table S3).
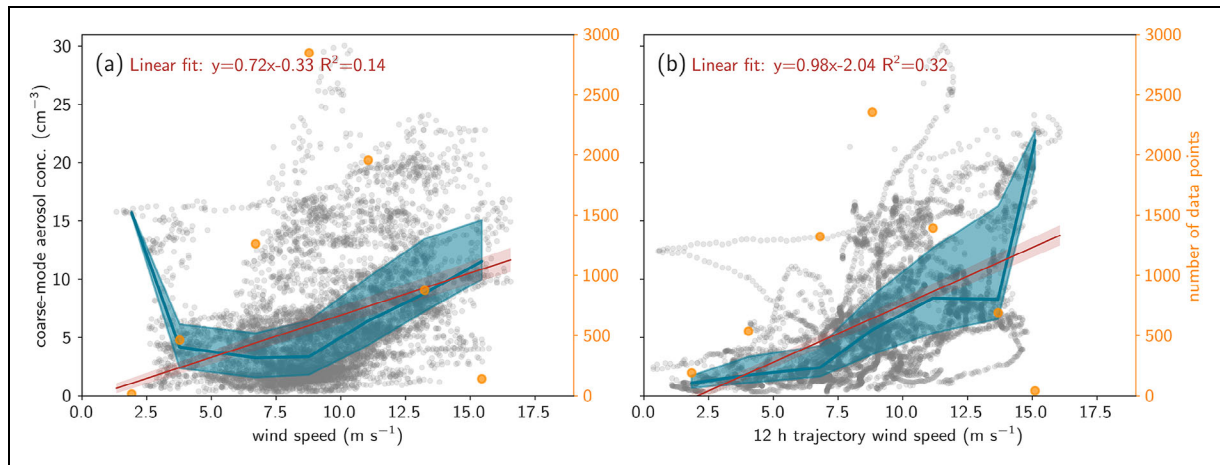
**Figure 3. Wind dependence of coarse-mode aerosol number concentrations during blowing snow events (BSEs).** Scatterplot with median (blue line) and interquartile range (shading) of coarse-mode aerosol concentrations during all BSEs against (a) in situ wind speed at RV *Polarstern*, and (b) trajectory wind speed 12 h before arrival at RV *Polarstern* grouped into bins of 2.5 m s$^{-1}$. The grey markers represent the underlying data. The orange markers (right axis) correspond to the number of data points per bin, note that the small number of data points for the smallest and largest bin make them less robust. The red line indicates a linear fit to the grey markers with $R^2$ showing the coefficient of determination (equal to $r_{Pearson}^2$). Other (nonlinear, stepwise linear) fits do not or only marginally improve $R^2$ (Figure S8, Figure S9). The correlation is unique to BSE periods and is not existent for non-BSE periods during November–May, as elevated wind speeds were rarely observed outside of BSEs (Figure S10).

The lack of significant correlation could potentially arise from the small sample size, or the complexity and nonlinearity of snow metamorphism, affecting blowing snow and aerosol emissions.

Given the importance of wind speed for coarse-mode aerosol number concentrations, we further explored whether the absolute values of local wind speed and trajectory wind speed can explain the variability of coarse-mode aerosol number concentrations (**Figure 3**). The correlation coefficient of coarse-mode aerosol concentration during BSEs with trajectory wind speed (12 h before arrival at RV *Polarstern*) is higher ($r_{spearman} = 0.63$, $P < 0.001$) than with local wind speed ($r_{spearman} = 0.52$, $P < 0.001$), and applying a linear fit, trajectory wind speed explains more variability in the coarse-mode aerosol number concentration (32%) compared to local wind speed (14%). This supports a regional source area of wind-sourced aerosol and suggests the importance of transported upwind generated SSaer or blowing snow particles. BSEs are associated with cyclonic systems (Rinke et al., 2021) with typical radii of about 500–1,300 km in the central Arctic (Valkonen et al., 2021). The highest correlation of coarse-mode aerosol number concentration with 9–12 h trajectory wind speed and a decline in the correlation coefficients for longer lead times (Figure S7) suggest a primary influence of a few hundred kilometers around RV *Polarstern* and therefore the sea ice covered area, as the distance to the sea ice edge between November and April was >800 km most of the time (Krumpen et al., 2021). This is consistent with the typical residence time of coarse-mode aerosol in such air masses (Seinfeld and Pandis, 2016). While the distance to the open ocean is large, open leads can be present closer to the location of RV *Polarstern* and contribute to SSaer emissions. Other variables that likely influence blowing snow occurrence and aerosol concentrations, including temperature, snowfall rate, snow drift density, snow age, and atmospheric boundary layer height, show only weak to moderate correlations with aerosol concentrations. A summary of correlation coefficients is provided in Table S3.

### 3.3. Seasonal cycle of coarse-mode aerosol and contribution of blowing snow events

The seasonal cycle of coarse-mode aerosol (1.06–16 μm $d_a$, **Figure 4a**) shows low median number concentrations in fall (0.19 cm$^{-3}$ in October), increases during winter with a peak in spring (4.15 cm$^{-3}$ in April) and the lowest concentration in summer (0.14 cm$^{-3}$ in August). The seasonal evolution is in line with Arctic haze that peaks in spring due to transport and accumulation of anthropogenic pollution (Quinn et al., 2007; Tunved et al., 2013), which also contributes to coarse-mode aerosol but at lower concentrations (Song et al., 2021). Compared to the seasonality of accumulation mode particles during MOSAiC (Boyer et al., 2023), coarse-mode aerosol concentrations peak later (April instead of January). In contrast to the coarse-mode aerosol number concentration in Svalbard from 2015–2019 (Song et al., 2021) that were obtained by the same model of aerodynamic particle sizer as during MOSAiC, our observations show higher values from November to April (by a factor of approximately 2.5–12) but comparable or lower values from June to September (factor of approximately 0.5–2.5). The higher values during polar night are interesting, given that MOSAiC took place in the central Arctic pack ice whereas Svalbard is located much closer to open ocean (approximately 30 km) where sea spray generation in the North Atlantic is known to significantly influence the aerosol population
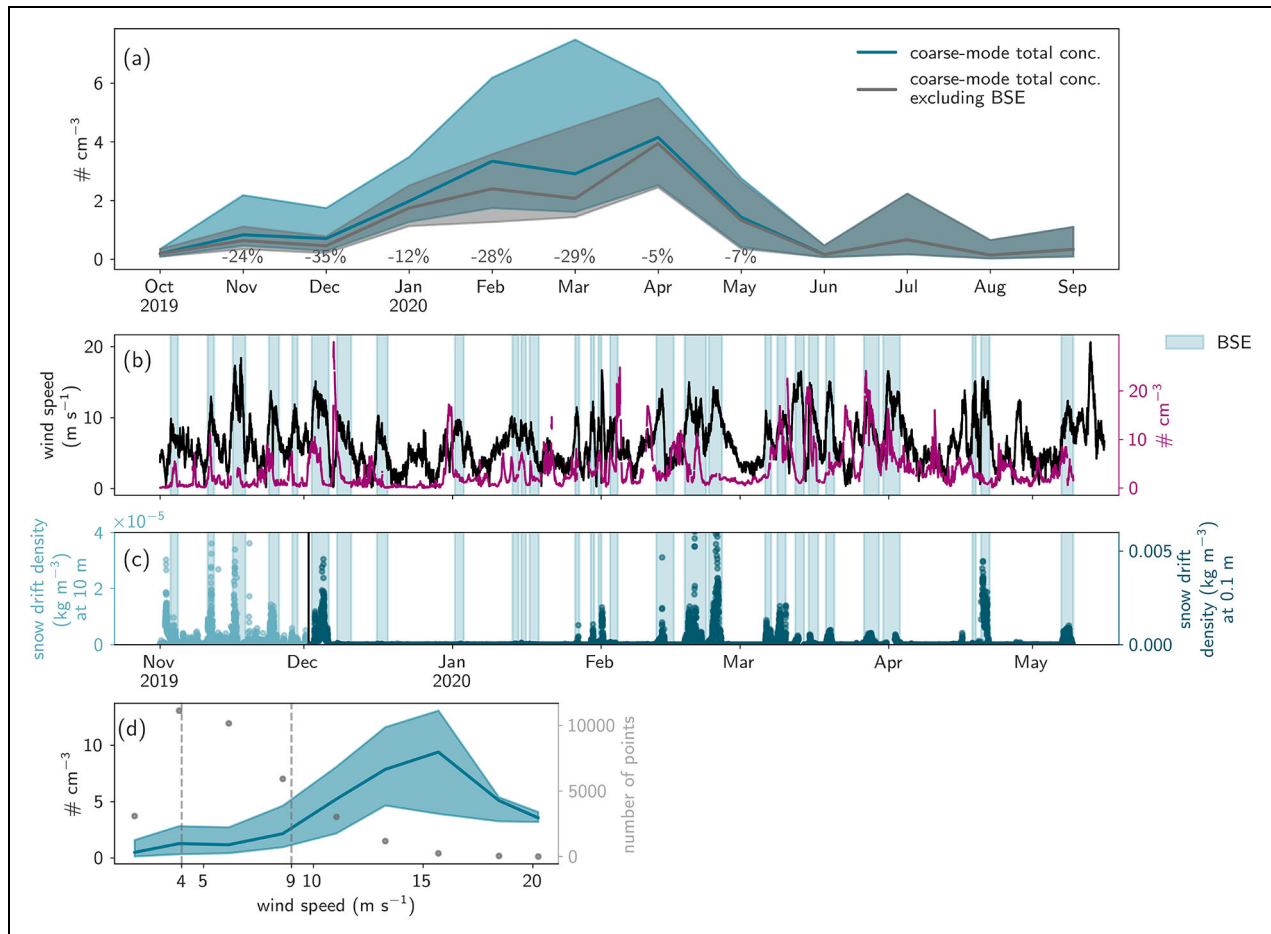
**Figure 4. Seasonal cycle of coarse-mode aerosol number concentrations.** (a) Seasonal cycle of coarse-mode aerosol total concentration (1.06–16 μm $d_a$) including and excluding blowing snow events (BSEs). The line shows median monthly concentration, the shading the interquartile range. The percentages describe the relative decrease of coarse-mode aerosol concentrations when excluding BSEs, calculated by (coarse-mode total conc. − coarse-mode total conc. excluding BSEs)/coarse-mode total conc. for each month. The monthly distributions with and without BSEs differ significantly from November–May based on a Mann-Whitney $U$ test. (b) 1 h averaged time series of coarse-mode total concentration, in situ wind speed and (c) the snow drift density at 10 m in November 2019 and at 0.1 m from December 2019 to May 15, 2020. The blue shaded area corresponds to the BSEs. (d) Median and interquartile range of coarse-mode aerosol total concentration from October to May as a function of in situ wind speed, grouped into bins of 2.5 m s$^{-1}$. The points indicate the number of data points per bin (right $y$-axis), note that the small number of data points for the largest bins make them less robust.

(Heslin-Rees et al., 2020). Potentially, coarse-mode aerosol concentrations during BSEs with number concentrations typically ranging from 2 to 8 cm$^{-3}$ (25th and 75th percentile, blue shading in **Figure 4b**) contribute to higher aerosol concentrations during polar night compared to Svalbard. However, we do not compare the same time period which may contribute to this difference.

BSEs occur almost a third of the time from November to mid-May during MOSAiC (**Figure 4b**, **c**), and the drop in occurrence between mid-March and mid-May could be due to various factors, such as reduced snowfall and lower wind speed, warmer temperatures and snow conditions less prone to drifting. Median monthly coarse-mode number concentrations decrease between 5% and 35% when excluding BSEs in the monthly median (blue vs. grey line in **Figure 4a**), with higher relative decreases in fall and winter. The reduced IQR in periods without BSEs (maximum IQR of 5.9 cm$^{-3}$

including BSEs vs. 3.1 cm$^{-3}$ without BSEs) suggests that BSEs contribute also considerably to coarse-mode aerosol concentration variability. Reductions of coarse-mode aerosol number concentrations during periods without BSEs are however upper-limit estimates as some BSEs coincide with long-range transport (Gong et al., 2023; Heutte et al., 2025) and coarse-mode aerosol originates from a mix of local and transported sources. As indicated in the previous sections, coarse-mode aerosol number concentrations show a clear dependency on wind speed (**Figure 4d**). Since coarse-mode number concentrations already start to increase for moderate wind speeds, we define the thresholds of <4 m s$^{-1}$ for low wind speed, and >9 m s$^{-1}$ for high wind speed (Frey et al., 2020; Chen et al., 2022) and use them to group data of high and low wind speed periods in the following sections.

From the high temporal resolution time series and the aerosol seasonal cycles including and excluding BSEs, we find
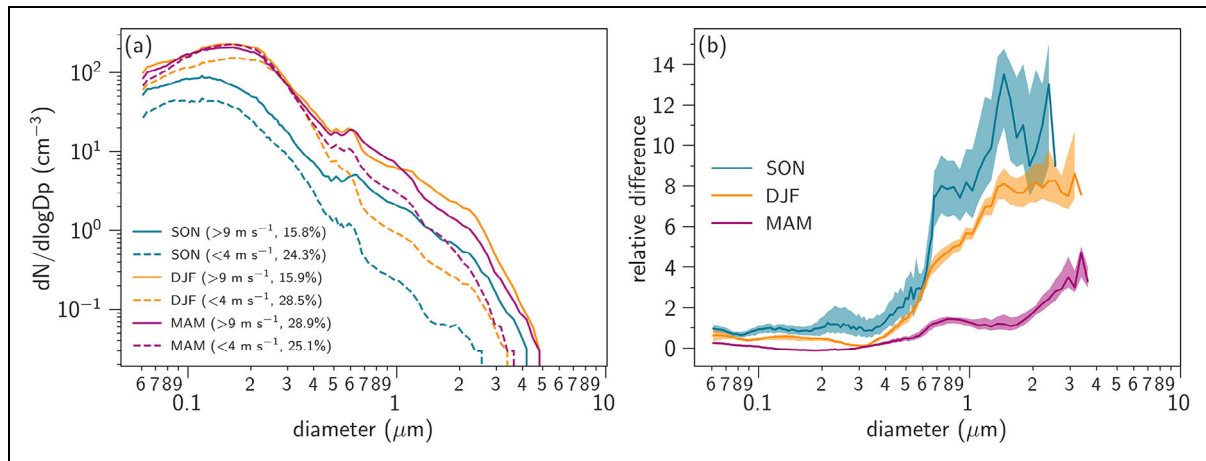
**Figure 5. Particle number size distributions during high and low wind.** (a) Median particle number size distributions ($d_{opt}$) for the categories high (>9 m s$^{-1}$) and low (<4 m s$^{-1}$) wind speed for each season (September–November, SON; December–February, DJF; March–May, MAM). Percentages indicate the percentage of time the condition is met during the respective season. (b) Relative difference calculated by dividing the difference of high and low wind speed median aerosol size distributions by the low wind median particle size distributions for each season from (a), where a relative difference of 1 indicates a 100% increase compared to the low wind speed concentrations. The shading denotes the 95% confidence intervals of bootstrapped relative differences (calculated by resampling high and low wind categories with replacement 1,000 times). Note that the "hump" at around 600 nm is not an actual mode but arises from the merging of the UHSAS and APS size distributions.

that high in situ wind speed and BSEs have an episodic, but notable contribution to the overall aerosol budget, with likely stronger contribution in the central Arctic compared to observations by Song et al. (2021) in Svalbard in winter.

### 3.4. Wind influence on aerosol properties
Given the dependence of aerosol concentration on wind speed during BSEs (Sections 3.1–3.3), we assessed aerosol size distributions, optical properties, CCN and INPs, and submicron NaCl more generally as a function of wind speed including seasonal differences.

#### 3.4.1. Aerosol size distributions
High wind speed leads to enhanced aerosol number concentrations across the whole size range in fall (September–November) and winter (December–February), and for most parts of the size distribution also in spring (March–May; except between around 100–300 nm) as shown in **Figure 5a** (Figure S11 includes the IQR and summer for comparison). In fall, the aerosol number concentrations are overall lower than in the other seasons (in line with Creamean et al., 2022), but high wind speed leads to almost a doubling for most parts of the size distribution. In spring, the increase of aerosol number concentrations from low to high wind speed is smaller (maximum absolute increase of 19 cm$^{-3}$ at 64 nm), which can be explained by elevated springtime background aerosol concentrations during Arctic haze. As shown in Gong et al. (2023), BSEs lead to large increases in fine-mode aerosol concentrations but the largest relative enhancements occur in the coarse-mode (**Figure 5b**). Relative enhancements are largest across most sizes for fall, second-largest for winter, and smallest for spring. For all seasons, relative enhancements particularly increase for particle sizes

>400 nm. Overall this shows that wind speed introduces coarse-mode particles but also increases fine-mode aerosol, even in the absence of BSEs (Figure S11).

The larger increases across the whole size distribution in fall and winter indicate a higher contribution of wind-sourced aerosol in these seasons. Increased number concentrations for all sizes have also been observed by Frey et al. (2020) in the Weddell sea over sea ice. In contrast, Chen et al. (2022) compared size distributions during blowing snow and non-blowing snow time periods during springtime in Utqiaġvik, Alaska. They found enhancements in the Aitken mode, but lower supermicron ($d_{opt}$) particle concentrations during blowing snow periods, suggesting that supermicron SSaer could be scavenged by blowing snow via electrophoretic attraction. Potentially, different conditions in the coastal Arctic influence the emission and scavenging of supermicron particles compared to the central Arctic, such as the presence of leads nearby in the coastal areas.

#### 3.4.2. Optical properties
In addition to impacting clouds, aerosols can directly interact with radiation by absorption and scattering. ARI depends on the aerosol chemical composition, size, and number concentrations. As discussed in Section 3.4.1, higher wind speeds correspond to increased total aerosol number concentrations, especially for the coarse-mode particles. The wind dependence is evident for supermicron aerosol (**Figures 6a**, **4d**) but less clear for submicron aerosol for moderate to high wind (5–15 m s$^{-1}$), potentially related to a higher aerosol baseline and smaller relative increase in particle concentration. Similar to the aerosol number concentrations, the total scattering coefficient for aerosol separated into <1 µm and <10 µm also
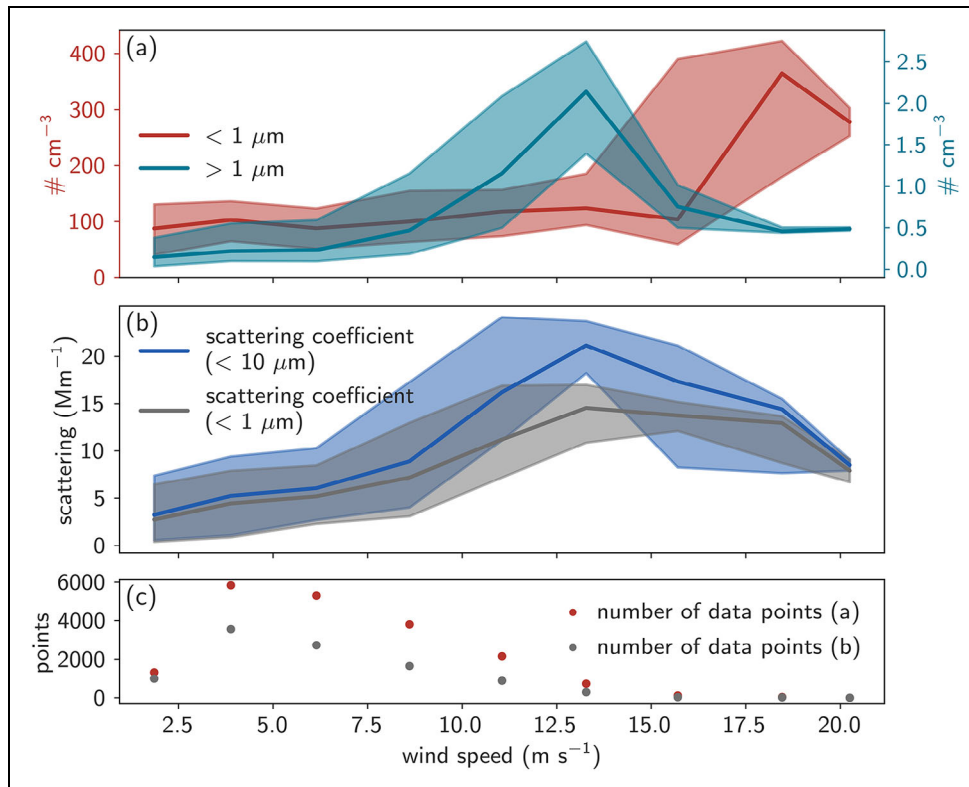
**Figure 6. Wind dependence of aerosol number concentrations and optical properties.** (a) Median (line) and interquartile range (shading) aerosol number concentrations for submicron and supermicron aerosol ($d_{\text{opt}}$) of the merged particle size distribution and (b) the total scattering coefficient for sub- and supermicron aerosol, as a function of in situ wind speed (grouped into bins of 2.5 m s$^{-1}$). The number of data points for each bin of the upper subfigures are given in (c), note that the small number of data points for the largest bins make them less robust.

increases with higher wind speed (**Figure 6b**). For higher wind speed (approximately 11–15 m s$^{-1}$), including supermicron aerosol in the scattering coefficient measurement enhances the scattering coefficient by a factor of approximately 1.5, showing that even though supermicron aerosol is two orders of magnitude lower in concentration than submicron aerosol, it strongly contributes to the scattering. The generation of scattering aerosol from blowing snow could impact radiative transfer in fall and spring, when twilight and daylight are present. We discuss the potential of a direct scattering effect of blowing snow aerosol in Section 3.5.

### 3.4.3. Submicron NaCl and seasonal wind speed dependence

The aerosol generated with high wind speed is hypothesized to primarily consist of SSaer from blowing snow and/or open leads (Yang et al., 2008; Huang and Jaeglé, 2017; Frey et al., 2020; Chen et al., 2022). Since chemical composition information for supermicron aerosol is not available, we estimated submicron NaCl levels using the AMS (Section 2.2.2) and compared them with coarse-mode aerosol concentrations. This is feasible, since wind-sourced aerosols span all size ranges (see Section 3.4.1). Submicron NaCl signal and total coarse-mode aerosol number concentrations show high correlations, and a linear fit can explain 79% of the variability in fall (**Figure 7a**) and 64% in spring (**Figure 7b**). This supports the

assumption that both total coarse-mode aerosol and submicron NaCl are generated by high wind speeds and suggests that coarse-mode aerosol is at least partially composed of sea salt particles. The explained variability is better in fall than in spring, and the slope is also higher in fall (0.03, in arbitrary units per number concentration) compared to spring (0.01, in arbitrary units per number concentration). We discuss potential reasons for the seasonal difference below.

In spring, elevated submicron NaCl levels were observed, when coarse-mode aerosol was not likely associated with local fresh sea spray emissions during May 12–13, 2020 (circled in **Figure 7b**), when large leads were open and visually observed in the immediate vicinity of RV *Polarstern* (Figure S12). The lower correlation but higher slope during this time period (0.02, **Figure 7b**) could indicate more submicron SSaer emissions from the local leads than from blowing snow, since sea spray has a dominant number concentration mode typically below 200 nm (Clarke et al., 2006; Quinn et al., 2015; Chen et al., 2022). Given the higher slope between NaCl and coarse-mode particles in fall compared to spring (**Figure 7a**), the May 12–13 observation can also potentially point to a more dominant influence from leads in fall. In addition, blowing snow could potentially generate larger particles than sea spray production. We test this hypothesis by comparing the median size distribution during all BSEs, during a BSE from December 2–6 and from May 7–9, with
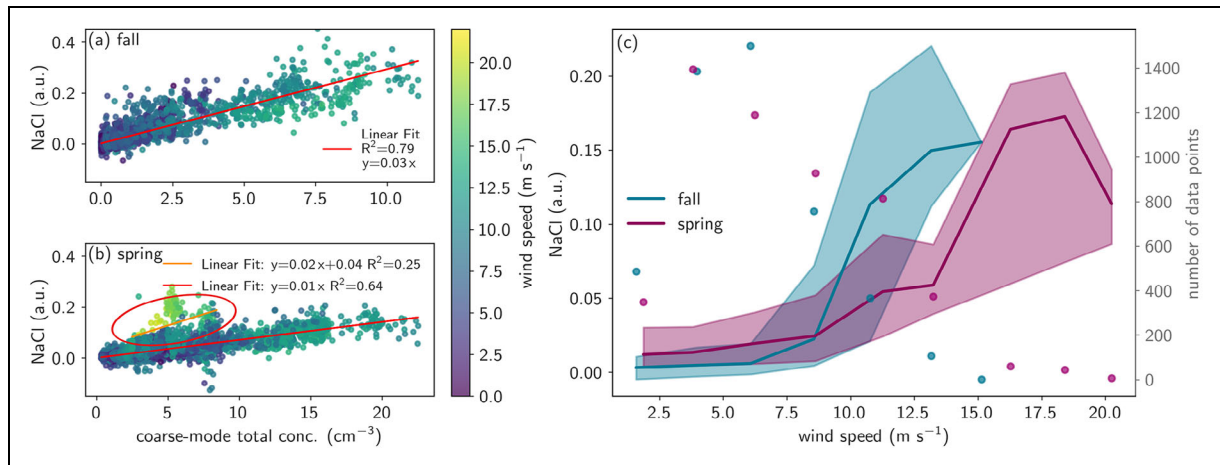
**Figure 7. NaCl levels and coarse-mode aerosol.** Correlation of coarse-mode aerosol total concentration and submicron NaCl levels for fall (a) and spring (b), when AMS data were available (all data have a time resolution of 10 min). The red circle in b indicates a high wind speed event on May 12–13, 2020 with extensive open leads around RV *Polarstern*. $R^2$ is the coefficient of determination (equal to $r_{Pearson}^2$) of the linear regression between the coarse-mode total concentration and submicron NaCl signal ($\times 51$). In (b), the linear fit is performed separately for the event with open leads (May 12–13) and the remaining data. (c) Median (line) and interquartile range (shading) submicron NaCl (AMS-based) as a function of in situ wind speed (grouped into bins of 2.5 m s$^{-1}$) for fall (October-beginning December, given the limited data availability of the AMS, we use all available data and include some days of December for fall) and spring (March–May). The colored points indicate the number of data points in each bin for fall and spring, respectively (right *y*-axis).

the event from May 12–13 (Figure S13). The size distribution from May 12–13 shows lower particle concentrations for diameters >2–3 μm compared to BSEs, but higher particle concentrations between 1 and 2 μm. However, further comparisons are needed, as other aerosols are likely present at the same time, and mixing heights and size-dependent removal rates likely vary across the events and influence the observed concentrations.

Investigating the relationship between wind speed and submicron NaCl (**Figure 7c**, Figure S14), we observe that for the same wind speed, submicron NaCl levels are higher in fall compared to spring (e.g., for 12–13 m s$^{-1}$: 0.16 a.u. in fall vs. 0.06 a.u. in spring). This could contribute to the higher slope of submicron NaCl versus coarse-mode particle number concentrations in fall (**Figure 7a**), and as also observed during the spring local lead event (**Figure 7b**). Snow salinities during MOSAiC also tend to be higher in fall and early winter than in spring (Figure S15, mean salinity in October–December 3.4 ppt compared to 1.9 ppt in March–May), which could likely be related to the salinity changes of sea ice with age and thickness (Cox and Weeks, 1974; Vancoppenolle et al., 2009), or chemical transformation processes particularly active in spring (e.g., Abbatt et al., 2012, Giordano et al., 2018).

We also compare the in situ wind speed dependence for fall, winter, and spring of different aerosol properties (**Figure 8**). While coarse-mode aerosol concentration increases for fall, winter, and spring with high wind speed, the concentrations are generally higher in spring, likely due to higher Arctic haze background concentrations in springtime, apart from concentrations at wind speed >15 m s$^{-1}$ in fall. To minimize the influence of Arctic haze,

we assess small Aitken mode particles (20–30 nm $d_m$), since they can also be produced by blowing snow sublimation (Yang et al., 2019; Heutte et al., 2025) or sea spray (Clarke et al., 2006; Myers et al., 2021; Xu et al., 2022). These ultrafine particles show stronger wind dependence in fall (**Figure 8d**), which would be consistent with higher fall SSaer emissions. Including slightly larger particles (20–60 nm $d_m$) shows a similar pattern, but a slightly smaller difference between fall and spring, likely due to the more significant Arctic haze influence in the larger size range (Figure S16). Also, the supermicron scattering coefficient shows a stronger dependence on wind speed in fall than in spring (**Figure 8b**), likely because of the salty coarse-mode aerosol generation with wind and the absence of the Arctic haze signal. On the contrary, it is smaller in spring and also less dependent on wind speed, which we interpret is due to the Arctic haze and lower availability of coarse-mode sea salt (with the assumption that supermicron NaCl shows a similar pattern as submicron NaCl). We also observe a dependence of the supermicron single scattering albedo (ω) on wind speed in fall and winter (**Figure 8c**), whereas in spring there is no correlation and ω values are generally high, again likely due to Arctic haze. The submicron scattering coefficients behave similarly against wind speed in fall, winter, and spring (up to 13 m s$^{-1}$, **Figure 8e**), except that the baseline is higher in winter and spring due to haze. The submicron ω is higher in fall and lowest in winter and increases in all 3 seasons with increasing wind speed (**Figure 8f**). This suggests that submicron aerosol in fall is more strongly influenced by SSaer, a highly scattering aerosol component, but less so in spring and winter during haze. Overall, we find that wind-generated particles
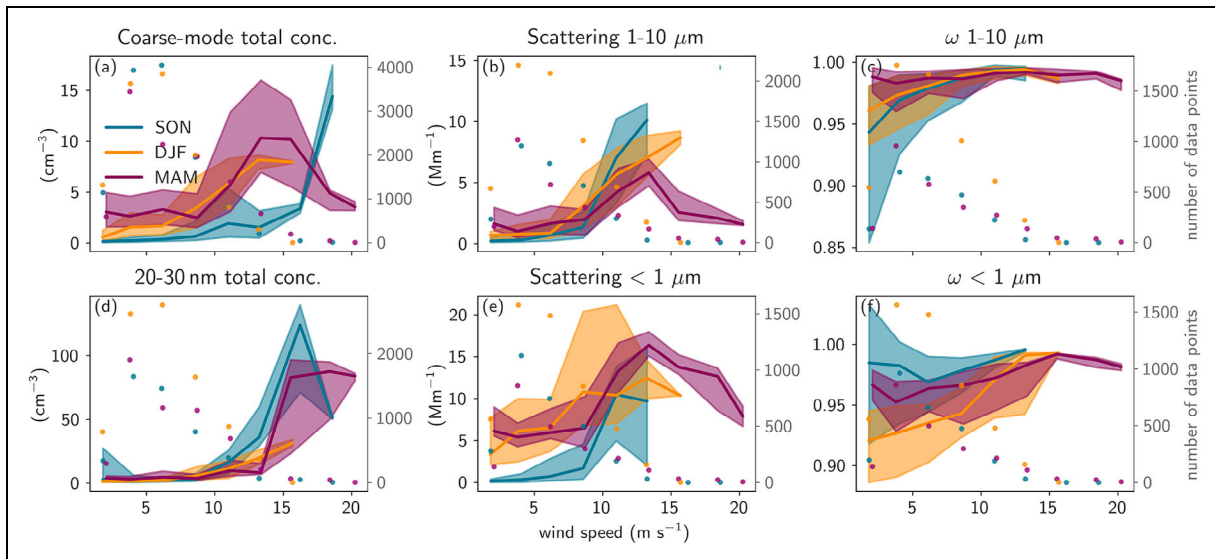
**Figure 8. Seasonal wind dependence of different aerosol properties.** Median (line) and interquartile range (shading) of different variables as a function of in situ wind speed (grouped into bins of 2.5 m s$^{-1}$) for fall (September–November, SON), winter (December–February, DJF), and spring (March–May, MAM) including (a) coarse-mode aerosol total number concentration, (b) the scattering coefficient for particles of 1–10 μm ($d_a$), the single scattering albedo (ω) for particles of 1–10 μm ($d_a$), (d) 20–30 nm ($d_m$) total number concentration, (e) the scattering coefficient for particles <1 μm ($d_a$), and (f) the ω for particles <1 μm ($d_a$). The colored points indicate the number of data points in each bin and variable for fall, winter, and spring, respectively (right y-axis).

have a stronger influence on submicron and supermicron scattering coefficients and ω in fall. During spring and partly also in winter, the influence of wind-generated particles is distinguishable but less significant because of Arctic haze.

Comparing the seasonal wind speed dependence of Aitken mode (20–30 nm $d_m$ in Figure S17, 20–60 nm $d_m$ in Figure S18) and accumulation mode particles (100–500 nm $d_m$ in Figure S19) during MOSAiC to other pan-Arctic stations (Figure S20) reveals large variability, indicating that pan-Arctic stations are not necessarily representative of the central Arctic regarding wind-sourced aerosol, possibly due to geographical location, source regions (i.e., distance to sea ice edge, open ocean, number, and size of leads), and atmospheric transport patterns. More details are provided in Section S3.4.

### 3.4.4. Influence on CCN and INPs

The climatic impact of aerosols largely depends on their influence on clouds, such as acting as CCN or INPs. Similar to the aerosol size distribution, CCN number concentrations are increased under high wind speed conditions with larger increases in fall compared to winter and spring where the smaller difference between high and low wind speed is likely due to haze conditions (**Figure 9a**). Since SSaer is an effective CCN, the CCN increase during high wind speed is consistent with the NaCl increase shown in Section 3.4.3 meaning that NaCl is likely an important contributor. The CCN baseline is lowest in fall with a median concentration of 16 cm$^{-3}$ at 0.3% but 90 cm$^{-3}$ at high wind. In clean conditions such as the Arctic in fall and early winter, cloud droplet number concentrations and cloud radiative forcing are sensitive to CCN concentrations (Garrett et al., 2002;

Garrett and Zhao, 2006; Mauritsen et al., 2011) and increased CCN concentrations could increase the long-wave emissivity of clouds and lead to surface warming. Indeed, Gong et al. (2023) estimated a net radiative forcing during cloudy days of +2.3 W m$^{-2}$ surface warming averaged from November to April by including a blowing snow source of SSaer in a global atmospheric transport model. Yet, this warming may differ from fall to spring, with likely larger contributions of blowing snow and wind-sourced CCN in fall and early winter.

In line with increased CCN concentrations and increased NaCl levels, which is hygroscopic (κ = 1.1; Zieger et al., 2017), the hygroscopicity parameter κ increases during high wind in all seasons (**Figure 9c**). The increase in κ is largest in fall and winter and we hypothesize that this is due to the observed low κ values of polar night haze when photooxidation is limited and the more hygroscopic secondary aerosol species (e.g., sulfuric acid, ammonium sulfate, oxygenated organics) may not yet play an important role for haze aerosol (Moschos et al., 2022; Schmale et al., 2022). Once sunlight is back, haze aerosol becomes more hygroscopic, and κ values increase.

In contrast to CCN, INP concentrations show no significant difference (based on a Student's $t$ test) between high and low wind speed conditions in each season, as shown in **Figure 9b** for INP concentrations at −20°C. This result does not depend on size nor temperature (−7.5°C to −25°C), even though springtime −25°C INP concentrations appear slightly higher during high wind speed. While there are individual high wind speed periods with enhanced INP concentrations, most BSEs do not show a systematic increase in INPs, suggesting that blowing snow is not a major source mechanism for
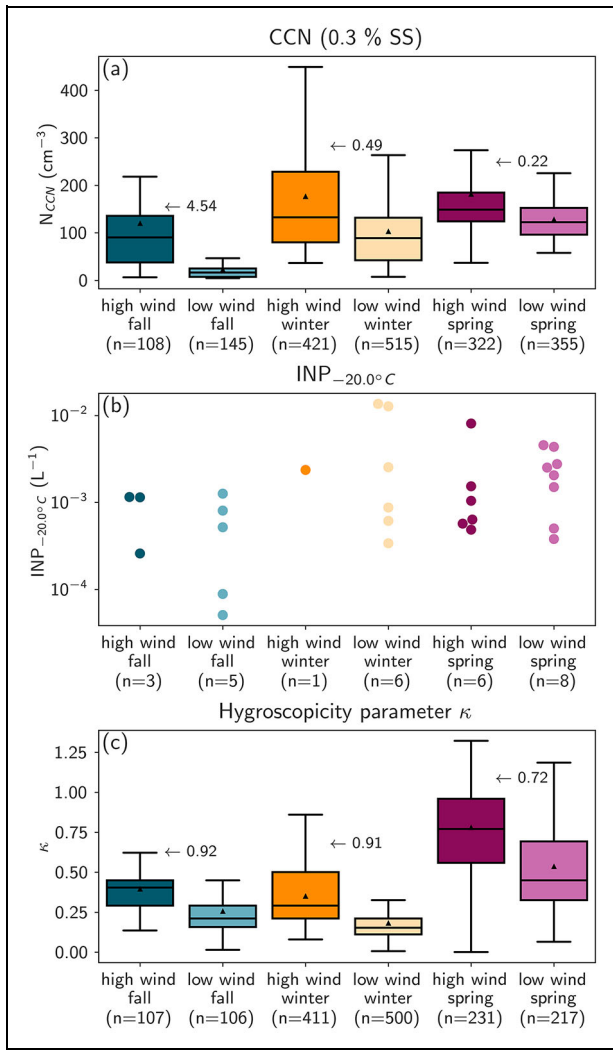
**Figure 9. CCN, INP, and hygroscopicity dependent on wind speed and season.** (a) Boxplots of CCN concentrations at 0.3% supersaturations for the categories high (>9 m s$^{-1}$) and low (<4 m s$^{-1}$) in situ wind speed for fall (September–November), winter (December–February), and spring (March–May). The mean CCN concentration is indicated with a triangle. (b) INP concentrations for the same categories as in a. (c) The hygroscopicity parameter kappa ($\kappa$) for 0.3% supersaturation for the same categories as in a and b. The annotated numbers for CCN and $\kappa$ boxplots indicate the relative enhancement of median values from low to high wind, for example, an enhancement of 4.54 indicates 454% higher concentrations compared to low wind speed.

freezing temperatures above −25°C according to these observations. Higher time resolution INP data could help to better identify potential correlations between INP concentration and wind speed. Here, only every third day has been analyzed for INPs. SSaer is a good CCN but can also act as INP, particularly in combination with organic material (DeMott et al., 2016; Alpert et al., 2022), even though SSaer is typically considered less effective than continental INP sources. While typical

INPs such as mineral dust and primary biological particles or other impurities can be present in the snow (Boetius et al., 2015) and transported dust likely contributed to higher INP concentrations in winter (Creamean et al., 2022), reemission of deposited INPs with wind speed is unlikely a dominant pathway based on the available data. Beck et al. (2024) observed increased hyperfluorescent aerosol with high wind speed but the fluorescence type associated with bacteria, a potential INP proxy, did not increase during blowing snow.

### 3.5. Potential climate-relevant impacts of wind-driven aerosol and recommendations for model evaluation

Wind-sourced and blowing snow aerosol and their contributions to CCN and scattering are relatively short-lived events (lasting from hours to days), but they occur on average once per week between November and mid-May (Section 3.3) and particles can be transported further away, possibly impacting the surface energy balance downwind. The estimated longwave effect of BSEs by Gong et al. (2023) demonstrates that these short-lived events could have a significant climatic impact. In addition to ACI, wind-sourced aerosol could also lead to ARI, and both aerosol climate effects likely vary throughout the seasons. **Figure 10** summarizes these potential climate impacts and related processes, with additional details in Section S4 including Figure S21 and Figure S22. In fall (**Figure 10a**), sea ice extent is at its minimum but expands as the season progresses. Given the climatologically high cloud coverage (Wang et al., 2021) and low aerosol number concentrations, ACI from increased CCN concentrations could be particularly important in fall and lead to enhanced cloud longwave emission. ARI could occur in early fall or in southern sea ice regions where daylight is present. In winter (**Figure 10b**), the area of frequent high wind over sea ice is largest (Figures S23, S24) but due to the lack of daylight, wind-sourced aerosol may primarily affect ACI, despite an increased aerosol concentration related to long-range transport in comparison to fall. ARI would only be possible in southern sea ice regions in late winter. In spring (**Figure 10c**), sea ice extent reaches its maximum and the area of frequent high wind remains high (Figures S23, S24). With an abundance of daylight, springtime could be the season where the possibility of a direct radiative effect of wind-sourced aerosol may be most relevant. Spring is also typically associated with the peak of Arctic haze (Schmale et al., 2022), yet the specific contributions of wind-sourced aerosol to ARI and ACI compared to Arctic haze remain to be quantified.

To further assess the climate effect of wind-sourced and blowing snow aerosol, model experiments are needed but require adequate representation of the source processes and resulting aerosol concentrations and properties. We suggest that our data can be primarily used to constrain, and evaluate modeling efforts. Given that the aerosol observations contain a mixed signal from various sources, we cannot unambiguously provide an SSaer or blowing
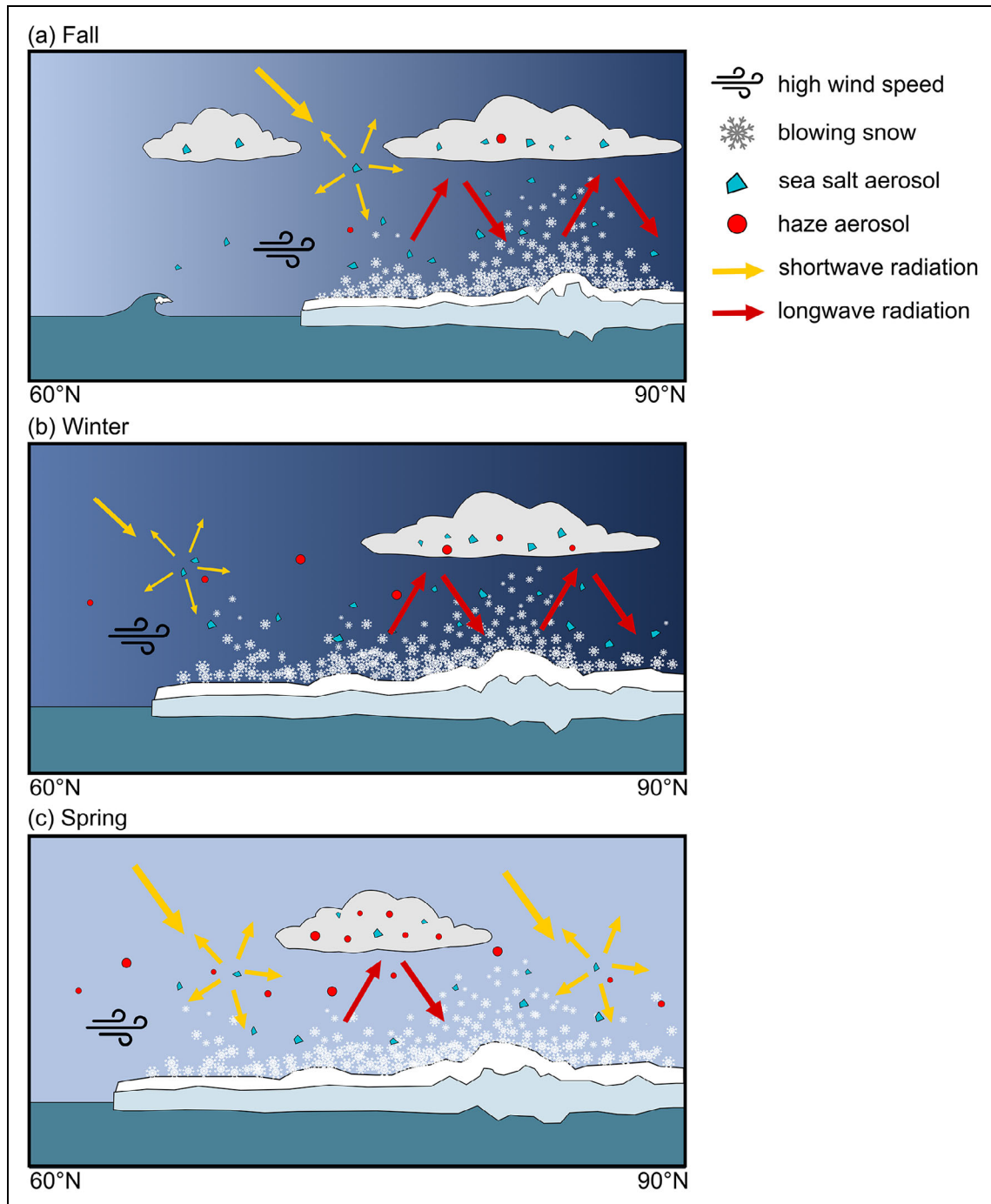
**Figure 10. Schematic of potential climate impacts of blowing snow and wind-sourced aerosol for fall, winter, and spring.** (a) Fall: lower sea ice extent, low Arctic haze aerosol, transition from polar day to polar night → wind-sourced aerosol could be most important for aerosol-cloud interaction (ACI), aerosol-radiation interaction (ARI) possible in the south. (b) Winter: high sea ice extent, Arctic haze aerosol increasing, polar night → wind-sourced aerosol could be important for ACI, only limited ARI possible in the south. (c) Spring: high sea ice extent, highest Arctic haze aerosol concentrations, daylight abundant → wind-sourced aerosol could be important for both ARI and ACI. The schematic is not to scale.

snow aerosol size distribution. However, the relative increase in different sizes between high wind and low wind (**Figure 5b**) could be compared to model size distributions including and excluding the blowing snow process. We suspect that the size distribution during high wind in fall (**Figure 5a**) has the highest contributions of SSaer given that the aerosol number concentration is lowest (Heutte et al., 2025), and could be compared to

the modeled SSaer size distribution. Coarse-mode aerosol emissions due to blowing snow could currently be underestimated as compared to leads (Lapere et al., 2024), given that we see more coarse-mode number concentration increases during BSEs than a local lead event (Section 3.4.3). While we report NaCl levels in arbitrary units, having applied the calibration factor by Ovadnevaite et al. (2012), the values should provide an order of

magnitude estimate for submicron NaCl mass concentrations (in µg m$^{-3}$) which can be compared to modeled submicron SSaer mass concentrations (**Figures 1** and **7**). Additionally, relative changes in CCN number concentrations or bulk hygroscopicity could be compared to our observed changes for different seasons (**Figure 9**).

## 4. Conclusions

In this study, we presented an overview of wind-sourced aerosol and specific aerosol properties as well as BSEs in the central Arctic from fall 2019 to spring 2020 based on measurements collected during the MOSAiC campaign. Our main findings can be summarized as follows:

- High wind speed and BSEs strongly enhance total aerosol concentrations, both fine-mode and coarse-mode particles, submicron NaCl and CCN concentrations, as well as bulk hygroscopicity, but not INP concentrations based on the available data. Potential longwave cloud forcing effects as reported in Gong et al. (2023) may be especially relevant in fall when generally the aerosol number concentration is low.
- SSaer concentrations and scattering properties react more strongly to wind speed in fall compared to spring, which may be related to higher contribution of open ocean sea spray, or shallower snowpacks and therefore higher salinities of the snow subject to drift in fall and early winter. Higher temporally resolved measurements of snowpack salinity, blowing snow salinity, and continuous NaCl measurements would be beneficial to further investigate this relationship as well as the influence of open leads across seasons.
- Increased coarse-mode aerosol number concentrations during high wind speed strongly enhance the scattering coefficient (factor 1.5) and potential impacts on radiative transfer are possible in fall in southern sea ice regions, but more likely in spring when daylight is more abundant. The possible influence on radiative transfer has so far not been assessed, and requires further investigations to quantify a potential effect, particularly during the haze season.
- BSE properties during MOSAiC are similar across all events with stronger relative aerosol enhancements in fall. Few BSEs with little/no enhancement compared to the baseline are likely related to older snow age (>6 days) before the BSEs. We can explain 32% of the coarse-mode aerosol variability by considering the 12 h trajectory wind speed, suggesting the importance of regional transport and consideration of air mass history prior to arrival at RV *Polarstern*. There is a weaker dependence on in situ wind speed, which explains only 14% of coarse-mode aerosol variability.
- Several cases show evidence of blowing snow heights reaching altitudes of up to almost 200 m and wind-sourced aerosol is likely present up to even higher altitudes in well-mixed boundary layers. Given the

high occurrence of cloud base heights below 300 m during MOSAiC, cloud influence of SSaer from blowing snow is expected.

The observations indicate that wind-sourced aerosol, such as sea spray aerosol and blowing snow SSaer, and the blowing snow process frequently occur in the central Arctic, and that this natural aerosol source likely has climatic relevance. Yet, further investigations are needed to quantify direct and indirect radiative effects as a function of season and their dependence on snow and sea ice properties. Quantifying the abundance of blowing snow versus sea spray aerosol and targeted measurements of lead and blowing snow emission fluxes could help to disentangle source contributions. This could help to further constrain the current natural aerosol baseline, and more quantitatively assess possible changes with climate change. Arctic amplification is highest in winter, and given the decline in anthropogenic aerosol, wind-sourced aerosol climatic effects will likely gain importance.

## Data availability statement

Aerosol number concentration from the APS: https://doi.pangaea.de/10.1594/PANGAEA.960923

Aerosol size distribution from the UHSAS: https://doi.org/10.5439/1409033

Aerosol size distribution from the SMPS: https://doi.org/10.5439/1476898

HR-ToF-AMS: https://doi.org/10.1594/PANGAEA.961009

CCN data: https://doi.org/10.5439/1323894

INP data: https://doi.org/10.5439/1804484

Aerosol optical properties: https://adc.arm.gov/metadata/epc/html/aosnephdry.html

Continuous meteorological surface measurements from RV *Polarstern*: https://doi.pangaea.de/10.1594/PANGAEA.935221; https://doi.pangaea.de/10.1594/PANGAEA.935222; https://doi.pangaea.de/10.1594/PANGAEA.935223; https://doi.pangaea.de/10.1594/PANGAEA.935224; https://doi.pangaea.de/10.1594/PANGAEA.935225

Continuous meteorological 10 m flux tower measurements: https://doi.org/10.18739/A2PV6B83F

Atmospheric boundary layer height: https://doi.pangaea.de/10.1594/PANGAEA.957760

Snowdrift data: https://doi.org/10.5285/7d8e401b-2c75-4ee4-a753-c24b7e91e6e9

Snow salinity profiles: https://doi.pangaea.de/10.1594/PANGAEA.946807

Sea ice extent: https://noaadata.apps.nsidc.org/NOAA/G02135/north/monthly/shapefiles/shp_extent/

Lidar data: https://polly.tropos.de/

Ceilometer data: https://doi.org/10.5439/1497398

## Supplemental files

The supplemental files for this article can be found as follows:

Supplementary Information: Tables S1–S3. Figures S1–S24. Texts S1–S4. Docx

## Competing interests
The authors declare that they have no competing interests. HA is associate editor at *Elementa* but she was not involved in the review process of this article.

## Author contributions
NB wrote the manuscript with input from JS, and all the authors provided comments/revisions. JS, IB, LLJQ, TL, TJ, JMC, MB, MMF, JU, ARM, MS, and GJ conducted MOSAiC field measurements reported in this work. SH lent and calibrated the CCNC. BH, NB, HA, IB, SRA, TJ, RE, and SYM provided and interpreted datasets with help from JBP, ML, JAM, KAP, XG, JW, TP, MK, and JS. JS obtained the funding and conceived the field measurements and this study for the *Swiss* Container during MOSAiC.

## References
**Abbatt, JPD, Thomas, JL, Abrahamsson, K, Boxe, C, Granfors, A, Jones, AE, King, MD, Saiz-Lopez, A, Shepson, PB, Sodeau, J, Toohey, DW, Toubin, C, von Glasow, R, Wren, SN, Yang, X.** 2012. Halogen activation via interactions with environmental ice and snow in the polar lower troposphere and other regions. *Atmospheric Chemistry and Physics* **12**(14): 6237–6271. DOI: http://dx.doi.org/10.5194/acp-12-6237-2012.

**Alpert, PA, Kilthau, WP, O'Brien, RE, Moffet, RC, Gilles, MK, Wang, B, Laskin, A, Aller, JY, Knopf, DA.** 2022. Ice-nucleating agents in sea spray aerosol identified and quantified with a holistic multimodal freezing model. *Science Advances* **8**(44): eabq6842. DOI: http://dx.doi.org/10.1126/sciadv.abq6842.

**Arctic Monitoring and Assessment Programme.** 2021. Arctic climate change update 2021: Key trends and impacts. Summary for Policy-makers. Tromsø, Norway: Arctic Monitoring and Assessment Programme (AMAP): 16. Available at https://www.amap.no/documents/doc/arctic-climate-change-update-2021-key-trends-and-impacts.-summary-for-policy-makers/3508. Accessed July 20, 2024.

**Beck, I, Angot, H, Baccarini, A, Dada, L, Quéléver, L, Jokinen, T, Laurila, T, Lampimäki, M, Bukowiecki, N, Boyer, M, Gong, X, Gysel-Beer, M, Petäjä, T, Wang, J, Schmale, J.** 2022. Automated identification of local contamination in remote atmospheric composition time series. *Atmospheric*

*Measurement Techniques* **15**(14): 4195–4224. DOI: http://dx.doi.org/10.5194/amt-15-4195-2022.

Beck, I, Angot, H, Baccarini, A, Lampimäki, M, Matthew, B, Schmale, J. 2021. Pollution detection algorithm (PDA). *EPEL* **1**: 1–7. DOI: http://dx.doi.org/10.5281/zenodo.5761101.

Beck, I, Moallemi, A, Heutte, B, Pernov, JB, Bergner, N, Rolo, M, Quéléver, LLJ, Laurila, T, Boyer, M, Jokinen, T, Angot, H, Hoppe, CJM, Müller, O, Creamean, J, Frey, MM, Freitas, G, Zinke, J, Salter, M, Zieger, P, Mirrielees, JA, Kempf, HE, Ault, AP, Pratt, KA, Gysel-Beer, M, Henning, S, Tatzelt, C, Schmale, J. 2024. Characteristics and sources of fluorescent aerosols in the central Arctic Ocean. *Elementa: Science of the Anthropocene* **12**(1): 00125. DOI: http://dx.doi.org/10.1525/elementa.2023.00125.

Boetius, A, Anesio, AM, Deming, JW, Mikucki, JA, Rapp, JZ. 2015. Microbial ecology of the cryosphere: Sea ice and glacial habitats. *Nature Reviews Microbiology* **13**(11): 677–690. DOI: http://dx.doi.org/10.1038/nrmicro3522.

Boyer, M, Aliaga, D, Pernov, JB, Angot, H, Quéléver, LLJ, Dada, L, Heutte, B, Dall'Osto, M, Beddows, DCS, Brasseur, Z, Beck, I, Bucci, S, Duetsch, M, Stohl, A, Laurila, T, Asmi, E, Massling, A, Thomas, DC, Nøjgaard, JK, Chan, T, Sharma, S, Tunved, P, Krejci, R, Hansson, HC, Bianchi, F, Lehtipalo, K, Wiedensohler, A, Weinhold, K, Kulmala, M, Petäjä, T, Sipilä, M, Schmale, J, Jokinen, T. 2023. A full year of aerosol size distribution data from the central Arctic under an extreme positive Arctic Oscillation: Insights from the Multidisciplinary drifting Observatory for the Study of Arctic Climate (MOSAiC) expedition. *Atmospheric Chemistry and Physics* **23**(1): 389–415. DOI: http://dx.doi.org/10.5194/acp-23-389-2023.

Carslaw, KS, Lee, LA, Reddington, CL, Pringle, KJ, Rap, A, Forster, PM, Mann, GW, Spracklen, DV, Woodhouse, MT, Regayre, LA, Pierce, JR. 2013. Large contribution of natural aerosols to uncertainty in indirect forcing. *Nature* **503**(7474): 67–71. DOI: http://dx.doi.org/10.1038/nature12674.

Charlson, RJ, Schwartz, SE, Hales, JM, Cess, RD, Coakley, JA, Hansen, JE, Hofmann, DJ. 1992. Climate forcing by anthropogenic aerosols. *Science* **255**(5043): 423–430. DOI: http://dx.doi.org/10.1126/science.255.5043.423.

Chen, Q, Mirrielees, JA, Thanekar, S, Loeb, NA, Kirpes, RM, Upchurch, LM, Barget, AJ, Lata, NN, Raso, ARW, McNamara, SM, China, S, Quinn, PK, Ault, AP, Kennedy, A, Shepson, PB, Fuentes, JD, Pratt, KA. 2022. Atmospheric particle abundance and sea salt aerosol observations in the springtime Arctic: A focus on blowing snow and leads. *Atmospheric Chemistry and Physics* **22**(23): 15263–15285. DOI: http://dx.doi.org/10.5194/acp-22-15263-2022.

Clarke, AD, Owens, SR, Zhou, J. 2006. An ultrafine sea-salt flux from breaking waves: Implications for cloud condensation nuclei in the remote marine atmosphere. *Journal of Geophysical Research: Atmospheres* **111**(D6). DOI: http://dx.doi.org/10.1029/2005JD006565.

Confer, KL, Jaeglé, L, Liston, GE, Sharma, S, Nandan, V, Yackel, J, Ewert, M, Horowitz, HM. 2023. Impact of changing Arctic sea ice extent, sea ice age, and snow depth on sea salt aerosol from blowing snow and the open ocean for 1980–2017. *Journal of Geophysical Research: Atmospheres* **128**(3): e2022JD037667. DOI: http://dx.doi.org/10.1029/2022JD037667.

Cox, CJ, Gallagher, MR, Shupe, MD, Persson, POG, Solomon, A, Fairall, CW, Ayers, T, Blomquist, B, Brooks, IM, Costa, D, Grachev, A, Gottas, D, Hutchings, JK, Kutchenreiter, M, Leach, J, Morris, SM, Morris, V, Osborn, J, Pezoa, S, Preußer, A, Riihimaki, LD, Uttal, T. 2023. Continuous observations of the surface energy budget and meteorology over the Arctic sea ice during MOSAiC. *Scientific Data* **10**(1): 519. DOI: http://dx.doi.org/10.1038/s41597-023-02415-5.

Cox, GFN, Weeks, WF. 1974. Salinity variations in sea ice. *Journal of Glaciology* **13**(67): 109–120. DOI: http://dx.doi.org/10.3189/S0022143000023418.

Creamean, JM, Barry, K, Hill, TCJ, Hume, C, DeMott, PJ, Shupe, MD, Dahlke, S, Willmes, S, Schmale, J, Beck, I, Hoppe, CJM, Fong, A, Chamberlain, E, Bowman, J, Scharien, R, Persson, O. 2022. Annual cycle observations of aerosols capable of ice formation in central Arctic clouds. *Nature Communications* **13**(1): 3537. DOI: http://dx.doi.org/10.1038/s41467-022-31182-x.

Croft, B, Martin, RV, Leaitch, WR, Tunved, P, Breider, TJ, D'Andrea, SD, Pierce, JR. 2016. Processes controlling the annual cycle of Arctic aerosol number and size distributions. *Atmospheric Chemistry and Physics* **16**(6): 3665–3682. DOI: http://dx.doi.org/10.5194/acp-16-3665-2016.

Curry, JA, Schramm, JL, Rossow, WB, Randall, D. 1996. Overview of Arctic cloud and radiation characteristics. *Journal of Climate* **9**(8): 1731–1764. DOI: http://dx.doi.org/10.1175/1520-0442(1996)009<1731:OOACAR>2.0.CO;2.

Dada, L, Angot, H, Beck, I, Baccarini, A, Quéléver, LLJ, Boyer, M, Laurila, T, Brasseur, Z, Jozef, G, de Boer, G, Shupe, MD, Henning, S, Bucci, S, Dütsch, M, Stohl, A, Petäjä, T, Daellenbach, KR, Jokinen, T, Schmale, J. 2022. A central arctic extreme aerosol event triggered by a warm air-mass intrusion. *Nature Communications* **13**(1): 1–15. DOI: http://dx.doi.org/10.1038/s41467-022-32872-2.

de Leeuw, G, Andreas, EL, Anguelova, MD, Fairall, CW, Lewis, ER, O'Dowd, C, Schulz, M, Schwartz, SE. 2011. Production flux of sea spray aerosol. *Reviews of Geophysics* **49**(2): 1–39. DOI: http://dx.doi.org/10.1029/2010RG000349.

DeMott, PJ, Hill, TCJ, McCluskey, CS, Prather, KA, Collins, DB, Sullivan, RC, Ruppel, MJ, Mason, RH, Irish, VE, Lee, T, Hwang, CY, Rhee, TS, Snider, JR, McMeeking, GR, Dhaniyala, S, Lewis, ER,

Wentzell, JJB, Abbatt, J, Lee, C, Sultana, CM, Ault, AP, Axson, JL, Diaz Martinez, M, Venero, I, Santos-Figueroa, G, Stokes, MD, Deane, GB, Mayol-Bracero, OL, Grassian, VH, Bertram, TH, Bertram, AK, Moffett, BF, Franc, GD. 2016. Sea spray aerosol as a unique source of ice nucleating particles. *Proceedings of the National Academy of Sciences* **113**(21): 5797–5803. DOI: http://dx.doi.org/10.1073/pnas.1514034112.

Doherty, SJ, Warren, SG, Grenfell, TC, Clarke, AD, Brandt, RE. 2010. Light-absorbing impurities in Arctic snow. *Atmospheric Chemistry and Physics* **10**(23): 11647–11680. DOI: http://dx.doi.org/10.5194/acp-10-11647-2010.

Domine, F, Sparapani, R, Ianniello, A, Beine, HJ. 2004. The origin of sea salt in snow on Arctic sea ice and in coastal regions. *Atmospheric Chemistry and Physics* **4**(9–10): 2259–2271. DOI: http://dx.doi.org/10.5194/acp-4-2259-2004.

Engelmann, R, Ansmann, A, Ohneiser, K, Griesche, H, Radenz, M, Hofer, J, Althausen, D, Dahlke, S, Maturilli, M, Veselovskii, I, Jimenez, C, Wiesen, R, Baars, H, Bühl, J, Gebauer, H, Haarig, M, Seifert, P, Wandinger, U, Macke, A. 2021. Wildfire smoke, Arctic haze, and aerosol effects on mixed-phase and cirrus clouds over the North Pole region during MOSAiC: An introduction. *Atmospheric Chemistry and Physics* **21**(17): 13397–13423. DOI: http://dx.doi.org/10.5194/acp-21-13397-2021.

Engelmann, R, Kanitz, T, Baars, H, Heese, B, Althausen, D, Skupin, A, Wandinger, U, Komppula, M, Stachlewska, IS, Amiridis, V, Marinou, E, Mattis, I, Linné, H, Ansmann, A. 2016. The automated multiwavelength Raman polarization and water-vapor lidar Polly$^{XT}$: The neXT generation. *Atmospheric Measurement Techniques* **9**(4): 1767–1784. DOI: http://dx.doi.org/10.5194/amt-9-1767-2016.

Feingold, G, Cotton, WR, Kreidenweis, SM, Davis, JT. 1999. The impact of giant cloud condensation nuclei on drizzle formation in stratocumulus: Implications for cloud radiative properties. *Journal of the Atmospheric Sciences* **56**(24): 4100–4117. DOI: http://dx.doi.org/10.1175/1520-0469(1999)056<4100:TIOGCC>2.0.CO;2.

Fetterer, F, Knowles, K, Meier, W, Savoie, M, Windnagel, A. 2017. *Sea ice index*. Boulder, CO. National Snow and Ice Data Center. DOI: http://dx.doi.org/10.7265/N5K072F8.

Freud, E, Krejci, R, Tunved, P, Leaitch, R, Nguyen, QT, Massling, A, Skov, H, Barrie, L. 2017. Pan-Arctic aerosol number size distributions: Seasonality and transport patterns. *Atmospheric Chemistry and Physics* **17**(13): 8101–8128. DOI: http://dx.doi.org/10.5194/acp-17-8101-2017.

Frey, MM, Norris, SJ, Brooks, IM, Anderson, PS, Nishimura, K, Yang, X, Jones, AE, Mastromonaco, MGN, Jones, DH, Wolff, EW. 2020. First direct observation of sea salt aerosol production from blowing snow above sea ice. *Atmospheric Chemistry and Physics* **20**(4): 2549–2578. DOI: http://dx.doi.org/10.5194/acp-20-2549-2020.

Garrett, TJ, Radke, LF, Hobbs, PV. 2002. Aerosol effects on cloud emissivity and surface longwave heating in the Arctic. *Journal of the Atmospheric Sciences* **59**(3): 769–778. DOI: http://dx.doi.org/10.1175/1520-0469(2002)059<0769:AEOCEA>2.0.CO;2.

Garrett, TJ, Zhao, C. 2006. Increased Arctic cloud longwave emissivity associated with pollution from mid-latitudes. *Nature* **440**(7085): 787–789. DOI: http://dx.doi.org/10.1038/nature04636.

Giordano, MR, Kalnajs, LE, Goetz, JD, Avery, AM, Katz, E, May, NW, Leemon, A, Mattson, C, Pratt, KA, DeCarlo, PF. 2018. The importance of blowing snow to halogen-containing aerosol in coastal Antarctica: Influence of source region versus wind speed. *Atmospheric Chemistry and Physics* **18**(22): 16689–16711. DOI: http://dx.doi.org/10.5194/acp-18-16689-2018.

Gong, X, Zhang, J, Croft, B, Yang, X, Frey, MM, Bergner, N, Chang, RYW, Creamean, JM, Kuang, C, Martin, RV, Ranjithkumar, A, Sedlacek, AJ, Uin, J, Willmes, S, Zawadowicz, MA, Pierce, JR, Shupe, MD, Schmale, J, Wang, J. 2023. Arctic warming by abundant fine sea salt aerosols from blowing snow. *Nature Geoscience* **16**(9): 768–774. DOI: http://dx.doi.org/10.1038/s41561-023-01254-8.

Gossart, A, Souverijns, N, Gorodetskaya, IV, Lhermitte, S, Lenaerts, JTM, Schween, JH, Mangold, A, Laffineur, Q, van Lipzig, NPM. 2017. Blowing snow detection from ground-based ceilometers: Application to East Antarctica. *The Cryosphere* **11**(6): 2755–2772. DOI: http://dx.doi.org/10.5194/tc-11-2755-2017.

Hansen, J, Nazarenko, L. 2004. Soot climate forcing via snow and ice albedos. *Proceedings of the National Academy of Sciences* **101**(2): 423–428. DOI: http://dx.doi.org/10.1073/pnas.2237157100.

Hersbach, H, Bell, B, Berrisford, P, Hirahara, S, Horányi, A, Muñoz-Sabater, J, Nicolas, J, Peubey, C, Radu, R, Schepers, D, Simmons, A, Soci, C, Abdalla, S, Abellan, X, Balsamo, G, Bechtold, P, Biavati, G, Bidlot, J, Bonavita, M, De Chiara, G, Dahlgren, P, Dee D, Diamantakis, M, Dragani, R, Flemming, J, Forbes, R, Fuentes, M, Geer, A, Haimberger, L, Healy, S, Hogan, RJ, Hólm, E, Janisková, M, Keeley, S, Laloyaux, P, Lopez, P, Lupu, C, Radnoti, G, de Rosnay, P, Rozum, I, Vamborg, F, Villaume, S, Thépaut, J-N. 2020. The ERA5 global reanalysis. *Quarterly Journal of the Royal Meteorological Society* **146**(730): 1999–2049. DOI: http://dx.doi.org/10.1002/qj.3803.

Heslin-Rees, D, Burgos, M, Hansson, H-C, Krejci, R, Ström, J, Tunved, P, Zieger, P. 2020. From a polar to a marine environment: Has the changing Arctic led to a shift in aerosol light scattering properties? *Atmospheric Chemistry and Physics* **20**(21): 13671–13686. DOI: http://dx.doi.org/10.5194/acp-20-13671-2020.

**Heutte, B, Bergner, N, Angot, H, Pernov, JB, Dada, L,** **Mirrielees, JA, Beck, I, Baccarini, A, Boyer, M,** **Creamean, JM, Daellenbach, KR, El Haddad, I,** **Frey MM, Henning, S, Laurila, T, Moschos, V,** **Petäjä, T, Pratt, KA, Quéléver, LLJ, Shupe, MD,** **Zieger, P, Jokinen, T, Schmale, J.** 2025. Observations of high time-resolution and size-resolved aerosol chemical composition and microphyscis in the central Arctic: Implications for climate-relevant particle properties. *Atmospheric Chemistry and Physics* **25**(4): 2207–2241. DOI: http://dx.doi.org/10.5194/acp-25-2207-2025.

**Heutte, B, Bergner, N, Beck, I, Angot, H, Dada, L, Qué-**léver, LLJ, Laurila, T, Boyer, M, Brasseur, Z, Daellenbach, KR, Henning, S, Kuang, C, Kulmala, M,** **Lampilahti, J, Lampimäki, M, Petäjä, T, Shupe,** **MD, Sipilä, M, Uin, J, Jokinen, T, Schmale, J.** 2023. Measurements of aerosol microphysical and chemical properties in the central Arctic atmosphere during MOSAiC. *Scientific Data* **10**(1): 690. DOI: http://dx.doi.org/10.1038/s41597-023-02586-1.

**Hovelsrud, GK, Poppel, B, van Oort, B, Reist, JD.** 2011. Arctic societies, cultures, and peoples in a changing cryosphere. *AMBIO* **40**(1): 100–110. DOI: http://dx.doi.org/10.1007/s13280-011-0219-4.

**Huang, J, Jaeglé, L.** 2017. Wintertime enhancements of sea salt aerosol in polar regions consistent with a sea ice source from blowing snow. *Atmospheric Chemistry and Physics* **17**(5): 3699–3712. DOI: http://dx.doi.org/10.5194/acp-17-3699-2017.

**Hyland, R, Wexler, A.** 1983. Formulations for the thermodynamic properties of the saturated phased of $H_2O$ from 173.15 to 473.15 K. *Ashrae Transactions* **89**(2): 500–520.

**Inoue, J, Sato, K, Rinke, A, Cassano, JJ, Fettweis, X,** **Heinemann, G, Matthes, H, Orr, A, Phillips, T,** **Seefeldt, M, Solomon, A, Webster, S.** 2021. Clouds and radiation processes in regional climate models evaluated using observations over the ice-free Arctic ocean. *Journal of Geophysical Research: Atmospheres* **126**(1): e2020JD033904. DOI: http://dx.doi.org/10.1029/2020JD033904.

**Itkin, P, Hendricks, S, Webster, M, von Albedyll, L,** **Arndt, S, Divine, D, Jaggi, M, Oggier, M, Raphael,** **I, Ricker, R, Rohde, J, Schneebeli, M, Liston, GE.** 2023. Sea ice and snow characteristics from yearlong transects at the MOSAiC Central Observatory. *Elementa: Science of the Anthropocene* **11**(1): 00048. DOI: http://dx.doi.org/10.1525/elementa.2022.00048.

**Jensen, JB, Nugent, AD.** 2017. Condensational growth of drops formed on giant sea-salt aerosol particles. *Journal of the Atmospheric Sciences* **74**(3): 679–697. DOI: http://dx.doi.org/10.1175/JAS-D-15-0370.1.

**Jozef, GC, Cassano, JJ, Dahlke, S, Dice, M, Cox, CJ, de** **Boer, G.** 2023a. Thermodynamic and kinematic drivers of atmospheric boundary layer stability in the central Arctic during the multidisciplinary drifting observatory for the study of Arctic climate (MOSAiC). *Atmospheric Chemistry and Physics* **23**(20): 13087–13106. DOI: http://dx.doi.org/10.5194/acp-23-13087-2023.

**Jozef, GC, Klingel, R, Cassano, JJ, Maronga, B, de Boer,** **G, Dahlke, S, Cox, CJ.** 2023b. Derivation and compilation of lower-atmospheric properties relating to temperature, wind, stability, moisture, and surface radiation budget over the central Arctic sea ice during MOSAiC. *Earth System Science Data* **15**(11): 4983–4995. DOI: http://dx.doi.org/10.5194/essd-15-4983-2023.

**Kaleschke, L, Richter, A, Burrows, J, Afe, O, Heygster,** **G, Notholt, J, Rankin, AM, Roscoe, HK, Hollwe-**del, J, Wagner, T, Jacobi, H-W.** 2004. Frost flowers on sea ice as a source of sea salt and their influence on tropospheric halogen chemistry. *Geophysical Research Letters* **31**(16): 1–4. DOI: http://dx.doi.org/10.1029/2004GL020655.

**Kirpes, RM, Bonanno, D, May, NW, Fraund, M, Barget,** **AJ, Moffet, RC, Ault, AP, Pratt, KA.** 2019. Wintertime Arctic sea spray aerosol composition controlled by sea ice lead microbiology. *ACS Central Science* **5**(11): 1760–1767. DOI: http://dx.doi.org/10.1021/acscentsci.9b00541.

**Knust, R.** 2017. Polar research and supply vessel POLARSTERN operated by the Alfred-Wegener-Institute. *Journal of Large-Scale Research Facilities JLSRF* **3**: A119. DOI: http://dx.doi.org/10.17815/jlsrf-3-163.

**Krumpen, T, von Albedyll, L, Goessling, HF, Hendricks,** **S, Juhls, B, Spreen, G, Willmes, S, Belter, HJ,** **Dethloff, K, Haas, C, Kaleschke, L, Katlein, C,** **Tian-Kunze, X, Ricker, R, Rostosky, P, Rückert,** **J, Singha, S, Sokolova, J.** 2021. MOSAiC drift expedition from October 2019 to July 2020: Sea ice conditions from space and comparison with previous years. *The Cryosphere* **15**(8): 3897–3920. DOI: http://dx.doi.org/10.5194/tc-15-3897-2021.

**Lapere, R, Marelle, L, Rampal, P, Brodeau, L, Melshei-**mer, C, Spreen, G, Thomas, JL.** 2024. Modeling the contribution of leads to sea spray aerosol in the high Arctic. *EGUsphere* **24**(21): 1–31. DOI: http://dx.doi.org/10.5194/egusphere-2024-1271.

**Lapere, R, Thomas, JL, Marelle, L, Ekman, AML, Frey,** **MM, Lund, MT, Makkonen, R, Ranjithkumar, A,** **Salter, ME, Samset, BH, Schulz, M, Sogacheva, L,** **Yang, X, Zieger, P.** 2023. The representation of sea salt aerosols and their role in polar climate within CMIP6. *Journal of Geophysical Research: Atmospheres* **128**(6): e2022JD038235. DOI: http://dx.doi.org/10.1029/2022JD038235.

**Legrand, M, Yang, X, Preunkert, S, Theys, N.** 2016. Yearround records of sea salt, gaseous, and particulate inorganic bromine in the atmospheric boundary layer at coastal (Dumont d'Urville) and central (Concordia) East Antarctic sites. *Journal of Geophysical Research: Atmospheres* **121**(2): 997–1023. DOI: http://dx.doi.org/10.1002/2015JD024066.

**Li, J, Carlson, BE, Yung, YL, Lv, D, Hansen, J, Penner, JE,** **Liao, H, Ramaswamy, V, Kahn, RA, Zhang, P,** **Dubovik, O, Ding, A, Lacis, AA, Zhang, L, Dong,**

**Y.** 2022. Scattering and absorbing aerosols in the climate system. *Nature Reviews Earth & Environment* **3**(6): 363–379. DOI: http://dx.doi.org/10.1038/s43017-022-00296-7.

**Li, L, Pomeroy, JW.** 1997. Probability of occurrence of blowing snow. *Journal of Geophysical Research: Atmospheres* **102**(D18): 21955–21964. DOI: http://dx.doi.org/10.1029/97JD01522.

**Loeb, NA, Kennedy, A.** 2021. Blowing snow at McMurdo station, Antarctica during the AWARE field campaign: Surface and ceilometer observations. *Journal of Geophysical Research: Atmospheres* **126**(7): e2020JD033935. DOI: http://dx.doi.org/10.1029/2020JD033935.

**Macfarlane, AR, Mellat, M, Dadic, R, Meyer, H, Werner, M, Brunello, C, Arndt, S, Krampe, D, Schneebeli, M.** 2023a. Ocean-sourced snow: An unaccounted process on Arctic sea ice. *Research Square* 1–36. DOI: http://dx.doi.org/10.21203/rs.3.rs-3572881/v1.

**Macfarlane, AR, Schneebeli, M, Dadic, R, Tavri, A, Immerz, A, Polashenski, C, Krampe, D, Clemens-Sewall, D, Wagner, DN, Perovich, DK, Henna-Reetta, H, Raphael, I, Matero, I, Regnery, J, Smith, MM, Nicolaus, M, Jaggi, M, Oggier, M, Webster, MA, Lehning, M, Kolabutin, N, Itkin, P, Naderpour, R, Pirazzini, R, Hämmerle, S, Arndt, S, Fons, S.** 2023b. A database of snow on sea ice in the central Arctic collected during the MOSAiC expedition. *Scientific Data* **10**(1): 398. DOI: http://dx.doi.org/10.1038/s41597-023-02273-1.

**Matrosov, SY.** 2024. Statistical relations among solid precipitation, atmospheric moisture and cloud parameters in the Arctic. *Atmosphere* **15**(1): 132. DOI: http://dx.doi.org/10.3390/atmos15010132.

**Mauritsen, T, Sedlar, J, Tjernström, M, Leck, C, Martin, M, Shupe, M, Sjogren, S, Sierau, B, Persson, POG, Brooks, IM, Swietlicki, E.** 2011. An Arctic CCN-limited cloud-aerosol regime. *Atmospheric Chemistry and Physics* **11**(1): 165–173. DOI: http://dx.doi.org/10.5194/acp-11-165-2011.

**May, NW, Quinn, PK, McNamara, SM, Pratt, KA.** 2016. Multiyear study of the dependence of sea salt aerosol on wind speed and sea ice conditions in the coastal Arctic. *Journal of Geophysical Research: Atmospheres* **121**(15): 9208–9219. DOI: http://dx.doi.org/10.1002/2016JD025273.

**Methven, J, Arnold, SR, O'Connor, FM, Barjat, H, Dewey, K, Kent, J, Brough, N.** 2003. Estimating photochemically produced ozone throughout a domain using flight data and a Lagrangian model. *Journal of Geophysical Research: Atmospheres* **108**(D9): 1–19. DOI: http://dx.doi.org/10.1029/2002JD002955.

**Mitchell, JM.** 1957. Visual range in the polar regions with particular reference to the Alaskan Arctic. *Journal of Atmospheric and Terrestrial Physics* **17**: 195–211.

**Moschos, V, Schmale, J, Aas, W, Becagli, S, Calzolai, G, Eleftheriadis, K, Moffett, CE, Schnelle-Kreis, J, Severi, M, Sharma, S, Skov, H, Vestenius, M, Zhang, W, Hakola, H, Hellén, H, Huang, L,** **Jaffrezo, J-L, Massling, A, Nøjgaard, JK, Petäjä, T, Popovicheva, O, Sheesley, RJ, Traversi, R, Yttri, KE, Prévôt, ASH, Baltensperger, U, Haddad, IE.** 2022. Elucidating the present-day chemical composition, seasonality and source regions of climate-relevant aerosols across the Arctic land surface. *Environmental Research Letters* **17**(3): 034032. DOI: http://dx.doi.org/10.1088/1748-9326/ac444b.

**Motos, G, Freitas, G, Georgakaki, P, Wieder, J, Li, G, Aas, W, Lunder, C, Krejci, R, Pasquier, JT, Henne-berger, J, David, RO, Ritter, C, Mohr, C, Zieger, P, Nenes, A.** 2023. Aerosol and dynamical contributions to cloud droplet formation in Arctic low-level clouds. *Atmospheric Chemistry and Physics* **23**(21): 13941–13956. DOI: http://dx.doi.org/10.5194/acp-23-13941-2023.

**Myers, DC, Lawler, MJ, Mauldin, RL, Sjostedt, S, Dubey, M, Abbatt, J, Smith, JN.** 2021. Indirect measurements of the composition of ultrafine particles in the Arctic late-winter. *Journal of Geophysical Research: Atmospheres* **126**(22): e2021JD035428. DOI: http://dx.doi.org/10.1029/2021JD035428.

**Nicolaus, M, Perovich, DK, Spreen, G, Granskog, MA, von Albedyll, L, Angelopoulos, M, Anhaus, P, Arndt, S, Belter, HJ, Bessonov, V, Birnbaum, G, Brauchle, J, Calmer, R, Cardellach, E, Cheng, B, Clemens-Sewall, D, Dadic, R, Damm, E, de Boer, G, Demir, O, Dethloff, K, Divine, DV, Fong, AA, Fons, S, Frey, MM, Fuchs, N, Gabarró, C, Gerland, S, Goessling, HF, Gradinger, R, Haapala, J, Haas, C, Hamilton, J, Hannula, H-R, Hendricks, S, Her-ber, A, Heuzé, C, Hoppmann, M, Høyland, KV, Huntemann, M, Hutchings, JK, Hwang, B, Itkin, P, Jacobi, H-W, Jaggi, M, Jutila, A, Kaleschke, L, Katlein, C, Kolabutin, N, Krampe, D, Kristensen, SS, Krumpen, T, Kurtz, N, Lampert, A, Lange, BA, Lei, R, Light, B, Linhardt, F, Liston, GE, Loose, B, Macfarlane, AR, Mahmud, M, Matero, IO, Maus, S, Morgenstern, A, Naderpour, R, Nandan, V, Niu-bom, A, Oggier, M, Oppelt, N, Pätzold, F, Perron, C, Petrovsky, T, Pirazzini, R, Polashenski, C, Rabe, B, Raphael, IA, Regnery, J, Rex, M, Ricker, R, Rie-mann-Campe, K, Rinke, A, Rohde, J, Salganik, E, Scharien, RK, Schiller, M, Schneebeli, M, Semml-ing, M, Shimanchuk, E, Shupe, MD, Smith, MM, Smolyanitsky, V, Sokolov, V, Stanton, T, Stroeve, J, Thielke, L, Timofeeva, A, Tonboe, RT, Tavri, A, Tsamados, M, Wagner, DN, Watkins, D, Webster, M, Wendisch, M.** 2022. Overview of the MOSAiC expedition: Snow and sea ice. *Elementa: Science of the Anthropocene* **10**(1): 000046. DOI: http://dx.doi.org/10.1525/elementa.2021.000046.

**Nishimura, K, Nemoto, M.** 2005. Blowing snow at Mizuho station, Antarctica. *Philosophical Transactions of the Royal Society A: Mathematical, Physical and Engineering Sciences* **363**(1832): 1647–1662. DOI: http://dx.doi.org/10.1098/rsta.2005.1599.

**Nishimura, K, Yokoyama, C, Ito, Y, Nemoto, M, Naaim-Bouvet, F, Bellot, H, Fujita, K.** 2014. Snow particle speeds in drifting snow. *Journal of Geophysical*

*Research: Atmospheres* **119**(16): 9901–9913. DOI: http://dx.doi.org/10.1002/2014JD021686.

Nixdorf, U, Dethloff, K, Rex, M, Shupe, M, Sommerfeld, A, Perovich, DK, Nicolaus, M, Heuzé C, Rabe, B, Loose, B, Damm, E, Gradinger, R, Fong, A, Maslowski, W, Rinke, A, Kwok, R, Spreen, G, Wendisch, M, Herber, A, Hirsekorn, M, Mohaupt, V, Frickenhaus, S, Immerz, A, Weiss-Tuider, K, König, B, Mengedoht, D, Regnery, J, Gerchow, P, Ransby, D, Krumpen, T, Morgenstern, A, Haas, C, Kanzow, T, Rack, FR, Saitzev, V, Sokolov, V, Makarov, A, Schwarze, S, Wunderlich, T, Wurr, K, Boetius, A. 2021. MOSAiC extended acknowledgement. *Zenodo.* DOI: http://dx.doi.org/10.5281/zenodo.5541624.

Ovadnevaite, J, Ceburnis, D, Canagaratna, M, Berresheim, H, Bialek, J, Martucci, G, Worsnop, DR, O'Dowd, C. 2012. On the effect of wind speed on submicron sea salt mass concentrations and source fluxes. *Journal of Geophysical Research: Atmospheres* **117**(D16): D16201. DOI: http://dx.doi.org/10.1029/2011JD017379.

Peng, S, Yang, Q, Shupe, MD, Xi, X, Han, B, Chen, D, Dahlke, S, Liu, C. 2023. The characteristics of atmospheric boundary layer height over the Arctic Ocean during MOSAiC. *Atmospheric Chemistry and Physics* **23**(15): 8683–8703. DOI: http://dx.doi.org/10.5194/acp-23-8683-2023.

Peterson, PK, Hartwig, M, May, NW, Schwartz, E, Rigor, I, Ermold, W, Steele, M, Morison, JH, Nghiem, SV, Pratt, KA. 2019. Snowpack measurements suggest role for multi-year sea ice regions in Arctic atmospheric bromine and chlorine chemistry. *Elementa: Science of the Anthropocene* **7**: 14. DOI: http://dx.doi.org/10.1525/elementa.352.

Petters, MD, Kreidenweis, SM. 2007. A single parameter representation of hygroscopic growth and cloud condensation nucleus activity. *Atmospheric Chemistry and Physics* **7**(8): 1961–1971. DOI: http://dx.doi.org/10.5194/acp-7-1961-2007.

Quinn, PK, Collins, DB, Grassian, VH, Prather, KA, Bates, TS. 2015. Chemistry and related properties of freshly emitted sea spray aerosol. *Chemical Reviews* **115**(10): 4383–4399. DOI: http://dx.doi.org/10.1021/cr500713g.

Quinn, PK, Shaw, G, Andrews, E, Dutton, EG, Ruoho-Airola, T, Gong, SL. 2007. Arctic haze: Current trends and knowledge gaps. *Tellus B: Chemical and Physical Meteorology* **59**(1): 99–114. DOI: http://dx.doi.org/10.1111/j.1600-0889.2006.00238.x.

Rabe, B, Heuzé, C, Regnery, J, Aksenov, Y, Allerholt, J, Athanase, M, Bai, Y, Basque, C, Bauch, D, Baumann, TM, Chen, D, Cole, ST, Craw, L, Davies, A, Damm, E, Dethloff, K, Divine, DV, Doglioni, F, Ebert, F, Fang, Y-C, Fer, I, Fong, AA, Gradinger, R, Granskog, MA, Graupner, R, Haas, C, He, H, He, Y, Hoppmann, M, Janout, M, Kadko, D, Kanzow, T, Karam, S, Kawaguchi, Y, Koenig, Z, Kong, B, Krishfield, RA, Krumpen, T, Kuhlmey, D, Kuznetsov, I, Lan, M, Laukert, G, Lei, R, Li, T, Torres-Valdés, S, Lin, L, Lin, L, Liu, H, Liu, N, Loose, B,

Ma, X, McKay, R, Mallet, M, Mallett, RDC, Maslowski, W, Mertens, C, Mohrholz, V, Muilwijk, M, Nicolaus, M, O'Brien, JK, Perovich, D, Ren, J, Rex, M, Ribeiro, N, Rinke, A, Schaffer, J, Schuffenhauer, I, Schulz, K, Shupe, MD, Shaw, W, Sokolov, V, Sommerfeld, A, Spreen, G, Stanton, T, Stephens, M, Su, J, Sukhikh, N, Sundfjord, A, Thomisch, K, Tippenhauer, S, Toole, JM, Vredenborg, M, Walter, M, Wang, H, Wang, L, Wang, Y, Wendisch, M, Zhao, J, Zhou, M, Zhu, J. 2022. Overview of the MOSAiC expedition: Physical oceanography. *Elementa: Science of the Anthropocene* **10**(1): 00062. DOI: http://dx.doi.org/10.1525/elementa.2021.00062.

Radke, LF, Hobbs, PV, Pinnons, JE. 1976. Observations of cloud condensation nuclei, sodium-containing particles, ice nuclei and the light-scattering coefficient near Barrow, Alaska. *Journal of Applied Meteorology and Climatology* **15**(9): 982–995. DOI: http://dx.doi.org/10.1175/1520-0450(1976)015<0982:OOCCNS>2.0.CO;2.

Ranjithkumar, A, Duncan, E, Yang, X, Partridge, D, Lachlan-Cope, T, Gong, X, Nishimura, K, Frey, MM. 2025. Direct observation of Arctic sea salt aerosol production from blowing snow and modelling over a changing sea ice environment. *Elementa: Science of the Anthropocene* **13**(1): 00006.

Rankin, AM, Auld, V, Wolff, EW. 2000. Frost flowers as a source of fractionated sea salt aerosol in the polar regions. *Geophysical Research Letters* **27**(21): 3469–3472. DOI: http://dx.doi.org/10.1029/2000GL011771.

Rankin, AM, Wolff, EW. 2003. A year-long record of size-segregated aerosol composition at Halley, Antarctica. *Journal of Geophysical Research: Atmospheres* **108**(D24): 1–12. DOI: http://dx.doi.org/10.1029/2003JD003993.

Rankin, AM, Wolff, EW, Martin, S. 2002. Frost flowers: Implications for tropospheric chemistry and ice core interpretation. *Journal of Geophysical Research: Atmospheres* **107**(D23): AAC 4-1–AAC 4-15. DOI: http://dx.doi.org/10.1029/2002JD002492.

Rantanen, M, Karpechko, AY, Lipponen, A, Nordling, K, Hyvärinen, O, Ruosteenoja, K, Vihma, T, Laaksonen, A. 2022. The Arctic has warmed nearly four times faster than the globe since 1979. *Communications Earth & Environment* **3**(1): 1–10. DOI: http://dx.doi.org/10.1038/s43247-022-00498-3.

Rhodes, RH, Yang, X, Wolff, EW, McConnell, JR, Frey, MM. 2017. Sea ice as a source of sea salt aerosol to Greenland ice cores: A model-based study. *Atmospheric Chemistry and Physics* **17**(15): 9417–9433. DOI: http://dx.doi.org/10.5194/acp-17-9417-2017.

Rinke, A, Cassano, JJ, Cassano, EN, Jaiser, R, Handorf, D. 2021. Meteorological conditions during the MOSAiC expedition: Normal or anomalous? *Elementa: Science of the Anthropocene* **9**(1): 00023. DOI: http://dx.doi.org/10.1525/elementa.2021.00023.

Roberts, GC, Nenes, A. 2005. A continuous-flow stream-wise thermal-gradient CCN chamber for atmospheric measurements. *Aerosol Science and Technology* **39**(3): 206–221. DOI: http://dx.doi.org/10.1080/027868290913988.

Roscoe, HK, Brooks, B, Jackson, AV, Smith, MH, Walker, SJ, Obbard, RW, Wolff, EW. 2011. Frost flowers in the laboratory: Growth, characteristics, aerosol, and the underlying sea ice. *Journal of Geophysical Research: Atmospheres* **116**(D12). DOI: http://dx.doi.org/10.1029/2010JD015144.

Salcedo, D, Onasch, TB, Dzepina, K, Canagaratna, MR, Zhang, Q, Huffman, JA, DeCarlo, PF, Jayne, JT, Mortimer, P, Worsnop, DR, Kolb, CE, Johnson, KS, Zuberi, B, Marr, LC, Volkamer, R, Molina, LT, Molina, MJ, Cardenas, B, Bernabé, RM, Márquez, C, Gaffney, JS, Marley, NA, Laskin, A, Shutthanandan, V, Xie, Y, Brune, W, Lesher, R, Shirley, T, Jimenez, JL. 2006. Characterization of ambient aerosols in Mexico City during the MCMA-2003 campaign with Aerosol Mass Spectrometry: Results from the CENICA Supersite. *Atmospheric Chemistry and Physics* **6**(4): 925–946. DOI: http://dx.doi.org/10.5194/acp-6-925-2006.

Schmale, J, Sharma, S, Decesari, S, Pernov, J, Massling, A, Hansson, H-C, von Salzen, K, Skov H, Andrews, E, Quinn, PK, Upchurch, LM, Eleftheriadis, K, Traversi, R, Gilardoni, S, Mazzola, M, Laing, J, Hopke, P. 2022. Pan-Arctic seasonal cycles and long-term trends of aerosol properties from 10 observatories. *Atmospheric Chemistry and Physics* **22**(5): 3067–3096. DOI: http://dx.doi.org/10.5194/acp-22-3067-2022.

Schmale, J, Zieger, P, Ekman, AML. 2021. Aerosols in current and future Arctic climate. *Nature Climate Change* **11**(2): 95–105. DOI: http://dx.doi.org/10.1038/s41558-020-00969-5.

Schmeisser, L, Backman, J, Ogren, JA, Andrews, E, Asmi, E, Starkweather, S, Uttal, T, Fiebig, M, Sharma, S, Eleftheriadis, K, Vratolis, S, Bergin, M, Tunved, P, Jefferson, A. 2018. Seasonality of aerosol optical properties in the Arctic. *Atmospheric Chemistry and Physics* **18**(16): 11599–11622. DOI: http://dx.doi.org/10.5194/acp-18-11599-2018.

Schmithüsen, H. 2021a. Continuous meteorological surface measurement during POLARSTERN cruise PS122/1 [dataset]. Bremerhaven, Germany: Alfred Wegener Institute, Helmholtz Centre for Polar and Marine Research, PANGAEA. DOI: http://dx.doi.org/10.1594/PANGAEA.935221.

Schmithüsen, H. 2021b. Continuous meteorological surface measurement during POLARSTERN cruise PS122/2 [dataset]. Bremerhaven, Germany: Alfred Wegener Institute, Helmholtz Centre for Polar and Marine Research, PANGAEA. DOI: http://dx.doi.org/10.1594/PANGAEA.935222.

Schmithüsen, H. 2021c. Continuous meteorological surface measurement during POLARSTERN cruise PS122/3 [dataset]. Bremerhaven, Germany: Alfred Wegener Institute, Helmholtz Centre for Polar and Marine Research, PANGAEA. DOI: http://dx.doi.org/10.1594/PANGAEA.935223.

Schmithüsen, H. 2021d. Continuous meteorological surface measurement during POLARSTERN cruise PS122/4 [dataset]. Bremerhaven, Germany: Alfred Wegener Institute, Helmholtz Centre for Polar and Marine Research, PANGAEA. DOI: http://dx.doi.org/10.1594/PANGAEA.935224.

Schmithüsen, H. 2021e. Continuous meteorological surface measurement during POLARSTERN cruise PS122/5 [dataset]. Bremerhaven, Germany: Alfred Wegener Institute, Helmholtz Centre for Polar and Marine Research, PANGAEA. DOI: http://dx.doi.org/10.1594/PANGAEA.935225.

Schuur, EAG, McGuire, AD, Schädel, C, Grosse, G, Harden, JW, Hayes, DJ, Hugelius, G, Koven, CD, Kuhry, P, Lawrence, DM, Natali, SM, Olefeldt, D, Romanovsky, VE, Schaefer, K, Turetsky, MR, Treat, CC, Vonk, JE. 2015. Climate change and the permafrost carbon feedback. *Nature* **520**(7546): 171–179. DOI: http://dx.doi.org/10.1038/nature14338.

Seinfeld, JH, Pandis, SN. 2016. *Atmospheric chemistry and physics: From air pollution to climate change.* Hoboken, NJ: John Wiley & Sons.

Shindell, D, Faluvegi, G. 2009. Climate response to regional radiative forcing during the twentieth century. *Nature Geoscience* **2**(4): 294–300. DOI: http://dx.doi.org/10.1038/ngeo473.

Shupe, MD, Intrieri, JM. 2004. Cloud radiative forcing of the Arctic surface: The influence of cloud properties, surface albedo, and solar zenith angle. *Journal of Climate* **17**(3): 616–628. DOI: http://dx.doi.org/10.1175/1520-0442(2004)017<0616:CRFOTA>2.0.CO;2.

Shupe, MD, Rex, M, Blomquist, B, Persson, POG, Schmale, J, Uttal, T, Althausen, D, Angot, H, Archer, S, Bariteau, L, Beck, I, Bilberry, J, Bucci, S, Buck, C, Boyer, M, Brasseur, Z, Brooks, IM, Calmer, R, Cassano, J, Castro, V, Chu, D, Costa, D, Cox, CJ, Creamean, J, Crewell, S, Dahlke, S, Damm, E, de Boer, G, Deckelmann, H, Dethloff, K, Dütsch, M, Ebell, K, Ehrlich, A, Ellis, J, Engelmann, R, Fong, AA, Frey, MM, Gallagher, MR, Ganzeveld, L, Gradinger, R, Graeser, J, Greenamyer, V, Griesche, H, Griffiths, S, Hamilton, J, Heinemann, G, Helmig, D, Herber, A, Heuzé, C, Hofer, J, Houchens, T, Howard, D, Inoue, J, Jacobi, H-W, Jaiser, R, Jokinen, T, Jourdan, O, Jozef, G, King, W, Kirchgaessner, A, Klingebiel, M, Krassovski, M, Krumpen, T, Lampert, A, Landing, W, Laurila, T, Lawrence, D, Lonardi, M, Loose, B, Lüpkes, C, Maahn, M, Macke, A, Maslowski, W, Marsay, C, Maturilli, M, Mech, M, Morris, S, Moser, M, Nicolaus, M, Ortega, P, Osborn, J, Pätzold, F, Perovich, DK, Petäjä, T, Pilz, C, Pirazzini, R, Posman, K, Powers, H, Pratt, KA, Preußer, A, Quéléver, L, Radenz, M, Rabe, B, Rinke, A, Sachs, T, Schulz, A, Siebert, H, Silva, T, Solomon, A, Sommerfeld, A, Spreen, G, Stephens, M, Stohl, A, Svensson, G, Uin, J, Viegas,

J, Voigt, C, von der Gathen, P, Wehner, B, Welker, JM, Wendisch, M, Werner, M, Xie, Z, Yue, F. 2022. Overview of the MOSAiC expedition: Atmosphere. *Elementa: Science of the Anthropocene* **10**(1): 00060. DOI: http://dx.doi.org/10.1525/elementa.2021.00060.

Solomon, A, Shupe, MD, Svensson, G, Barton, NP, Batrak, Y, Bazile, E, Day, JJ, Doyle, JD, Frank, HP, Keeley, S, Remes, T, Tolstykh, M. 2023. The winter central Arctic surface energy budget: A model evaluation using observations from the MOSAiC campaign. *Elementa: Science of the Anthropocene* **11**(1): 00104. DOI: http://dx.doi.org/10.1525/elementa.2022.00104.

Song, C, Dall'Osto, M, Lupi, A, Mazzola, M, Traversi, R, Becagli, S, Gilardoni, S, Vratolis, S, Yttri, KE, Beddows, DCS, Schmale, J, Brean, J, Kramawijaya, AG, Harrison, RM, Shi, Z. 2021. Differentiation of coarse-mode anthropogenic, marine and dust particles in the High Arctic islands of Svalbard. *Atmospheric Chemistry and Physics* **21**(14): 11317–11335. DOI: http://dx.doi.org/10.5194/acp-21-11317-2021.

Stohl, A. 2006. Characteristics of atmospheric transport into the Arctic troposphere. *Journal of Geophysical Research* **111**(D11): D11306. DOI: http://dx.doi.org/10.1029/2005JD006888.

Taylor, PC, Boeke, RC, Li, Y, Thompson, DWJ. 2019. Arctic cloud annual cycle biases in climate models. *Atmospheric Chemistry and Physics* **19**(13): 8759–8782. DOI: http://dx.doi.org/10.5194/acp-19-8759-2019.

Tunved, P, Ström, J, Krejci, R. 2013. Arctic aerosol life cycle: Linking aerosol size distributions observed between 2000 and 2010 with air mass transport and precipitation at Zeppelin station, Ny-Ålesund, Svalbard. *Atmospheric Chemistry and Physics* **13**(7): 3643–3660. DOI: http://dx.doi.org/10.5194/acp-13-3643-2013.

Uin, J, Aiken, AC, Dubey, MK, Kuang, C, Pekour, M, Salwen, C, Sedlacek, AJ, Senum, G, Smith, S, Wang, J, Watson, TB, Springston, SR. 2019. Atmospheric Radiation Measurement (ARM) Aerosol Observing Systems (AOS) for surface-based in situ atmospheric aerosol and trace gas measurements. *Journal of Atmospheric and Oceanic Technology* **36**(12): 2429–2447. DOI: http://dx.doi.org/10.1175/JTECH-D-19-0077.1.

Valkonen, E, Cassano, J, Cassano, E. 2021. Arctic cyclones and their interactions with the declining sea ice: A recent climatology. *Journal of Geophysical Research: Atmospheres* **126**(12): e2020JD034366. DOI: http://dx.doi.org/10.1029/2020JD034366.

Vancoppenolle, M, Fichefet, T, Goosse, H. 2009. Simulating the mass balance and salinity of Arctic and Antarctic sea ice. 2. Importance of sea ice salinity variations. *Ocean Modelling* **27**(1–2): 54–69. DOI: http://dx.doi.org/10.1016/j.ocemod.2008.11.003.

von Albedyll, L, Hendricks, S, Grodofzig, R, Krumpen, T, Arndt, S, Belter, HJ, Birnbaum, G, Cheng, B, Hoppmann, M, Hutchings, J, Itkin, P, Lei, R, Nicolaus, M, Ricker, R, Rohde, J, Suhrhoff, M,

Timofeeva, A, Watkins, D, Webster, M, Haas, C. 2022. Thermodynamic and dynamic contributions to seasonal Arctic sea ice thickness distributions from airborne observations. *Elementa: Science of the Anthropocene* **10**(1): 00074. DOI: http://dx.doi.org/10.1525/elementa.2021.00074.

von Albedyll, L, Hendricks, S, Hutter, N, Murashkin, D, Kaleschke, L, Willmes, S, Thielke, L, Tian-Kunze, X, Spreen, G, Haas, C. 2024. Lead fractions from SAR-derived sea ice divergence during MOSAiC. *The Cryosphere* **18**(3): 1259–1285. DOI: http://dx.doi.org/10.5194/tc-18-1259-2024.

von Salzen, K, Whaley, CH, Anenberg, SC, Van Dingenen, R, Klimont, Z, Flanner, MG, Mahmood, R, Arnold, SR, Beagley, S, Chien, R-Y, Christensen, JH, Eckhardt, S, Ekman, AML, Evangeliou, N, Faluvegi, G, Fu, JS, Gauss, M, Gong, W, Hjorth, JL, Im, U, Krishnan, S, Kupiainen, K, Kühn, T, Langner, J, Law, KS, Marelle, L, Olivié, D, Onishi, T, Oshima, N, Paunu, V-V, Peng, Y, Plummer, D, Pozzoli, L, Rao, S, Raut, J-C, Sand, M, Schmale, J, Sigmond, M, Thomas, MA, Tsigaridis, K, Tsyro, S, Turnock, ST, Wang, M, Winter, B. 2022. Clean air policies are key for successfully mitigating Arctic warming. *Communications Earth & Environment* **3**(1): 1–11. DOI: http://dx.doi.org/10.1038/s43247-022-00555-x.

Wagenbach, D, Ducroz, F, Mulvaney, R, Keck, L, Minikin, A, Legrand, M, Hall, JS, Wolff, EW. 1998. Sea-salt aerosol in coastal Antarctic regions. *Journal of Geophysical Research: Atmospheres* **103**(D9): 10961–10974. DOI: http://dx.doi.org/10.1029/97JD01804.

Wang, X, Liu, J, Yang, B, Bao, Y, Petropoulos, GP, Liu, H, Hu, B. 2021. Seasonal trends in clouds and radiation over the Arctic seas from satellite observations during 1982 to 2019. *Remote Sensing* **13**(16): 3201. DOI: http://dx.doi.org/10.3390/rs13163201.

Wei, J, Wang, Z, Gu, M, Luo, J-J, Wang, Y. 2021. An evaluation of the Arctic clouds and surface radiative fluxes in CMIP6 models. *Acta Oceanologica Sinica* **40**(1): 85–102. DOI: http://dx.doi.org/10.1007/s13131-021-1705-6.

Willis, MD, Leaitch, WR, Abbatt, JPD. 2018. Processes controlling the composition and abundance of Arctic aerosol. *Reviews of Geophysics* **56**(4): 621–671. DOI: http://dx.doi.org/10.1029/2018RG000602.

Xu, W, Ovadnevaite, J, Fossum, KN, Lin, C, Huang, R-J, Ceburnis, D, O'Dowd, C. 2022. Sea spray as an obscured source for marine cloud nuclei. *Nature Geoscience* **15**(4): 282–286. DOI: http://dx.doi.org/10.1038/s41561-022-00917-2.

Yang, X, Frey, MM, Rhodes, RH, Norris, SJ, Brooks, IM, Anderson, PS, Nishimura, K, Jones, AE, Wolff, EW. 2019. Sea salt aerosol production via sublimating wind-blown saline snow particles over sea ice: Parameterizations and relevant microphysical mechanisms. *Atmospheric Chemistry and Physics* **19**(13): 8407–8424. DOI: http://dx.doi.org/10.5194/acp-19-8407-2019.

**Yang, X**, **Neděla, V**, **Runštuk, J**, **Ondrušková, G**, **Krausko, J**, **Vetráková, Ľ**, **Heger, D.** 2017. Evaporating brine from frost flowers with electron microscopy and implications for atmospheric chemistry and sea-salt aerosol formation. *Atmospheric Chemistry and Physics* **17**(10): 6291–6303. DOI: http://dx.doi.org/10.5194/acp-17-6291-2017.

**Yang, X**, **Pyle, JA**, **Cox, RA.** 2008. Sea salt aerosol production and bromine release: Role of snow on sea ice. *Geophysical Research Letters* **35**(16): L16815. DOI: http://dx.doi.org/10.1029/2008GL034536.

**Zhao, C**, **Garrett, T.** 2014. Effects of Arctic haze on surface cloud radiative forcing. *Geophysical Research Letters* **42**(2): 557–564. DOI: http://dx.doi.org/10.1002/2014GL062015.

**Zieger, P**, **Väisänen, O**, **Corbin, JC**, **Partridge, DG**, **Bastelberger, S**, **Mousavi-Fard, M**, **Rosati, B**, **Gysel, M**, **Krieger, UK**, **Leck, C**, **Nenes, A**, **Riipinen, I**, **Virtanen, A**, **Salter, ME.** 2017. Revising the hygroscopicity of inorganic sea salt particles. *Nature Communications* **8**(1): 15883. DOI: http://dx.doi.org/10.1038/ncomms15883.